ISSN 0352-9045

Informacije MIDEM

Journal of Microelectronics, Electronic Components and Materials
Vol. 53, No. 4(2023), December 2023

Revija za mikroelektroniko, elektronske sestavne dele in materiale
letnik 53, številka 4(2023), December 2023

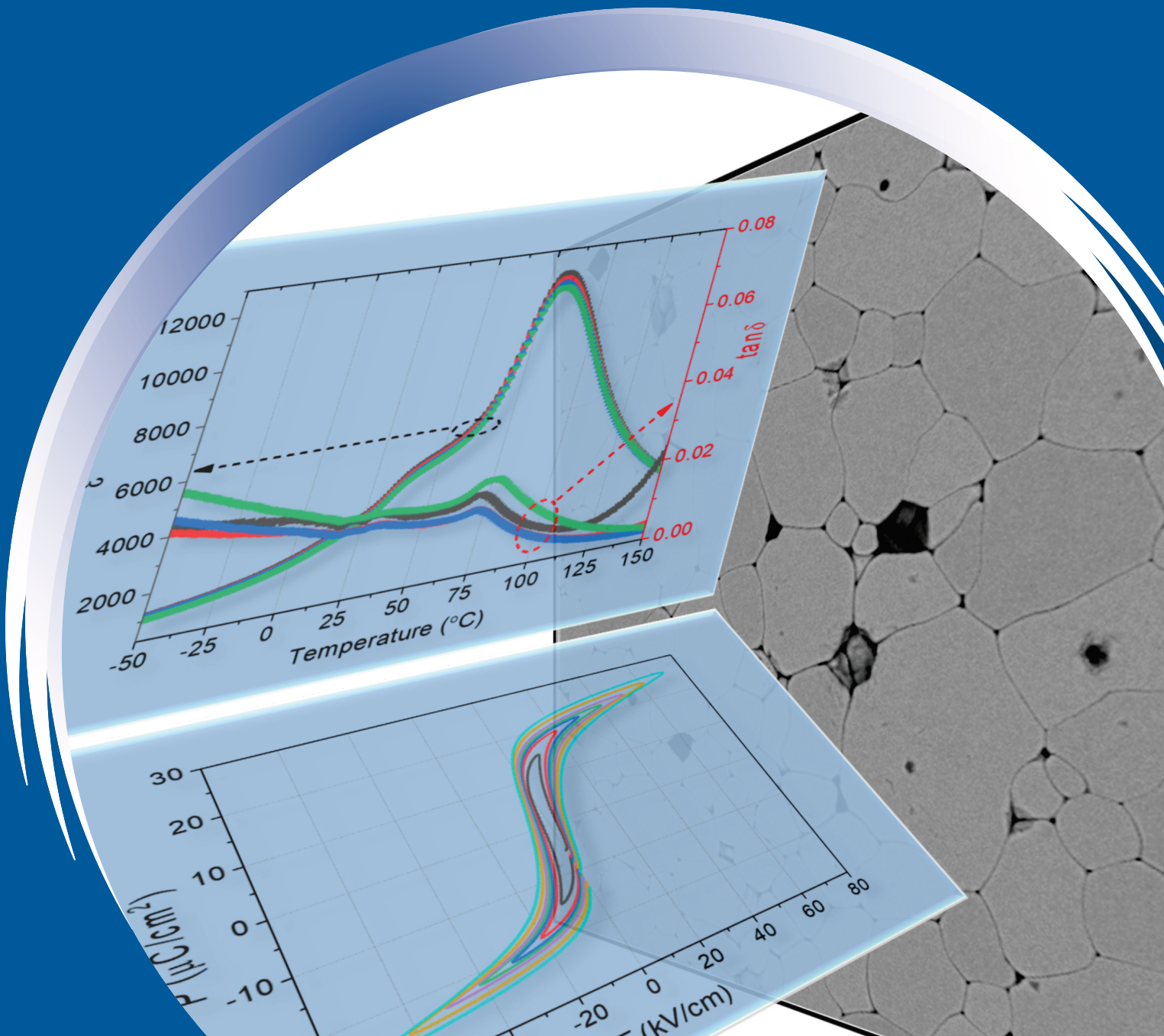

UDK 621.3:(53+54+621+66)(05)(497.1)=00 ISSN 0352-9045

Informacije MIDEM *4-2023*

Journal of Microelectronics, Electronic Components and Materials

VOLUME 53, NO. 4(188), LJUBLJANA, DECEMBER 2023 | LETNIK 53, NO. 4(188), LJUBLJANA, DECEMBER 2023

Published quarterly (March, June, September, December) by Society for Microelectronics, Electronic Components and Materials - MIDEM.
Copyright © 2023. All rights reserved. | Revija izhaja trimesečno (marec, junij, september, december). Izdaja Strokovno društvo za mikroelektroniko, elektronske sestavne dele in materiale – Društvo MIDEM. Copyright © 2023. Vse pravice pridržane.

Editor in Chief | Glavni in odgovorni urednik
Marko Topič, University of Ljubljana (UL), Faculty of Electrical Engineering, Slovenia

Editor of Electronic Edition | Urednik elektronske izdaje
Kristijan Brecl, UL, Faculty of Electrical Engineering, Slovenia

Associate Editors | Odgovorni področni uredniki
Vanja Ambrožič, UL, Faculty of Electrical Engineering, Slovenia
Arpad Bürmen, UL, Faculty of Electrical Engineering, Slovenia
Danjela Kuščer Hrovatin, Jožef Stefan Institute, Slovenia
Matija Pirc, UL, Faculty of Electrical Engineering, Slovenia
Franc Smole, UL, Faculty of Electrical Engineering, Slovenia
Matjaž Vidmar, UL, Faculty of Electrical Engineering, Slovenia

Editorial Board | Uredniški odbor
Mohamed Akil, ESIEE PARIS, France
Giuseppe Buja, University of Padova, Italy
Gian-Franco Dalla Betta, University of Trento, Italy
Martyn Fice, University College London, United Kingdom
Ciprian Iliescu, Institute of Bioengineering and Nanotechnology, A*STAR, Singapore
Marc Lethiecq, University of Tours, France
Teresa Orlowska-Kowalska, Wroclaw University of Technology, Poland
Luca Palmieri, University of Padova, Italy
Goran Stojanović, University of Novi Sad, Serbia

International Advisory Board | Časopisni svet
Janez Trontelj, UL, Faculty of Electrical Engineering, Slovenia - Chairman
Cor Claeys, IMEC, Leuven, Belgium
Denis Đonlagić, University of Maribor, Faculty of Elec. Eng. and Computer Science, Slovenia
Zvonko Fazarinc, CIS, Stanford University, Stanford, USA
Leszek J. Golonka, Technical University Wroclaw, Wroclaw, Poland
Jean-Marie Haussonne, EIC-LUSAC, Octeville, France
Barbara Malič, Jožef Stefan Institute, Slovenia
Miran Mozetič, Jožef Stefan Institute, Slovenia
Stane Pejovnik, UL, Faculty of Chemistry and Chemical Technology, Slovenia
Giorgio Pignatel, University of Perugia, Italy
Giovanni Soncini, University of Trento, Trento, Italy
Iztok Šorli, MIKROIKS d.o.o., Ljubljana, Slovenia
Hong Wang, Xi´an Jiaotong University, China

Headquarters | Naslov uredništva
Uredništvo Informacije MIDEM
MIDEM pri MIKROIKS
Stegne 11, 1521 Ljubljana, Slovenia
T. +386 (0)1 513 37 68
F. + 386 (0)1 513 37 71
E. info@midem-drustvo.si
www.midem-drustvo.si

Annual subscription rate is 160 EUR, separate issue is 40 EUR. MIDEM members and Society sponsors receive current issues for free. Scientific Council for Technical Sciences of Slovenian Research Agency has recognized Informacije MIDEM as scientific Journal for microelectronics, electronic components and materials. Publishing of the Journal is co-financed by Slovenian Research Agency and by Society sponsors. Scientific and professional papers published in the journal are indexed and abstracted in COBISS and INSPEC databases. The Journal is indexed by ISI® for Sci Search®, Research Alert® and Material Science Citation Index™. |
Letna naročnina je 160 EUR, cena posamezne številke pa 40 EUR. Člani in sponzorji MIDEM prejemajo posamezne številke brezplačno. Znanstveni svet za tehnične vede je podal pozitivno mnenje o reviji kot znanstveno-strokovni reviji za mikroelektroniko, elektronske sestavne dele in materiale. Izdajo revije sofinancirajo ARRS in sponzorji društva. Znanstveno-strokovne prispevke objavljene v Informacijah MIDEM zajemamo v podatkovne baze COBISS in INSPEC. Prispevke iz revije zajema ISI® v naslednje svoje produkte: Sci Search®, Research Alert® in Materials Science Citation Index™.

Design | Oblikovanje: Snežana Madić Lešnik; Printed by | tisk: Biro M, Ljubljana; Circulation | Naklada: 1000 issues | izvodov; Slovenia Taxe Percue | Poštnina plačana pri pošti 1102 Ljubljana

Informacije MIDEM
Journal of Microelectronics,
Electronic Components and Materials
vol. 53, No. 4(2023)

Content | Vsebina

Original scientific papers — Izvirni znanstveni članki

Review scientific papers — Pregledni znanstveni članki

Original scientific paper
https://doi.org/10.33180/InfMIDEM2023.401

Informacije MIDEM
Journal of Microelectronics,
Electronic Components and Materials
Vol. 53, No. 4(2023), 207 – 223

Virtual Reference Tag Assisted Radio Frequency Identification Localization and Tracking Using Artificial Intellect Techniques in Indoor Environment

Mathavan Nagaraj[1], Siva Ranjani Seenivasan[2]

[1]Department of Electronics &Communication Engineering, Nadar Saraswathi College of Engineering and Technology, Vadapudupatti, Theni, Tamil Nadu, India.
[2]Department of Computer Science and Engineering, Sethu Institute of Technology, Tamil Nadu, India.

Abstract: The application of Radio Frequency Identification (RFID) technology for localizing and tracking mobile objects within indoor environments, primarily relying on Received Signal Strength Indicator (RSSI) readings, poses challenges in enhancing tracking accuracy and minimizing errors. In response, we present the VIRALTRACK (Virtual Reference Tag Localization and Tracking) model, comprising four key processes: signal improvement, optimization-based virtual reference tag allocation, quantum-based localization, and deep reinforcement learning-based tracking. The Extended Gradient Filter (EGF) algorithm is introduced to mitigate RSSI fluctuations, thereby enhancing signal efficiency. The Emperor Penguin Colony (EPC) optimization algorithm allocates virtual reference tags, factoring in Signal-to-Noise Ratio (SNR), tag quantity, and environmental conditions, elevating tracking accuracy. Quantum Neural Network (QNN) facilitates precise position estimation for moving targets, with the SignRank algorithm optimizing virtual reference tag selection to reduce tracking errors. The Twin Delayed Deep Deterministic Policy Gradient (TD3) algorithm ensures effective tracking by considering distance, phase, orientation, and previous coordinates. Simulations conducted using the NS3.26 network simulator evaluate performance metrics, including tracking accuracy, tracking error, and cumulative probability, validating the efficacy of the proposed VIRALTRACK model in RFID-based indoor localization and tracking.

Keywords: Radio Frequency Identification (RFID), Virtual Reference Tag Allocation, RFID reader, Quantum Neural Network (QNN), Extended Gradient Filter (EGF)

Radiofrekvenčna identifikacija, lokalizacija in sledenje s pomočjo virtualne referenčne oznake z uporabo tehnik umetne inteligence v notranjem okolju

Izvleček: Uporaba tehnologije radiofrekvenčne identifikacije (RFID) za lociranje in sledenje mobilnih predmetov v notranjih okoljih, ki temelji predvsem na odčitkih indikatorja moči sprejetega signala (RSSI), predstavlja izziv pri izboljšanju natančnosti sledenja in zmanjšanju napak. V odgovor na to predstavljamo model VIRALTRACK (Virtual Reference Tag Localization and Tracking), ki vključuje štiri ključne postopke: izboljšanje signala, dodeljevanje virtualnih referenčnih oznak na podlagi optimizacije, lokalizacijo na podlagi kvantne metode in sledenje na podlagi globokega učenja z okrepitvijo. Uveden je algoritem EGF (Extended Gradient Filter), ki ublaži nihanja RSSI in s tem izboljša učinkovitost signala. Optimizacijski algoritem Emperor Penguin Colony (EPC) dodeljuje virtualne referenčne oznake ob upoštevanju razmerja med signalom in šumom (SNR), količine oznak in okoljskih pogojev, kar povečuje natančnost sledenja. Kvantno nevronsko omrežje (QNN) omogoča natančno ocenjevanje položaja premikajočih se ciljev, algoritem SignRank pa optimizira izbiro navideznih referenčnih oznak, da zmanjša napake pri sledenju. Algoritem TD3 (Twin Delayed Deep Deterministic Policy Gradient) zagotavlja učinkovito sledenje z upoštevanjem razdalje, faze, orientacije in prejšnjih koordinat. Simulacije, izvedene z omrežnim simulatorjem NS3.26, ocenjujejo kazalnike učinkovitosti, vključno z natančnostjo sledenja, napako sledenja in kumulativno verjetnostjo, kar potrjuje učinkovitost predlaganega modela VIRALTRACK pri notranji lokalizaciji in sledenju na podlagi RFID.

Ključne besede: Radiofrekvenčna identifikacija (RFID), dodeljevanje virtualnih referenčnih oznak, bralnik RFID, kvantno nevronsko omrežje (QNN), razširjeni gradientni filter (EGF)

** Corresponding Author's e-mail: mathavann2022@gmail.com*

How to cite:
M. Nagaraj et al., "Virtual Reference Tag Assisted Radio Frequency Identification Localization and Tracking Using Artificial Intellect Techniques in Indoor Environment", Inf. Midem-J. Microelectron. Electron. Compon. Mater., Vol. 53, No. 3(2023), pp. 207–223

1 Introduction

Automatic localization and tracking technologies have garnered significant attention, driven by the increasing prevalence of location-based applications. This is particularly crucial in scenarios such as logistics management and construction worker supervision, where real-time indoor localization and tracking of moving targets play a pivotal role. The conventional Global Positioning System (GPS) faces limitations in indoor tracking due to issues such as signal blocking and non-line-of-sight conditions [1-3]. As a result, Radio Frequency Identification (RFID)-based tracking technology has emerged as a promising solution, showcasing adaptability to large-scale indoor environments and effectiveness in non-line-of-sight conditions [4-5]. In the realm of RFID-based tracking systems, the fundamental components include RFID tags and readers. RFID readers are employed to collect Received Signal Strength Indicator (RSSI) information from moving target tags, fostering communication and enabling the localization and tracking of the target within indoor environments [6-7]. Indoor localization using RFID technology can be categorized into range-free and range-based approaches [8]. The former utilizes connection information like hop size and anchor position, while the latter incorporates distance estimation between the transmitter and receiver for communication [9-10]. Range-based approaches have demonstrated superiority in large-scale scenarios, leveraging precise tag selection based on RSSI [11]. RFID tags are classified into passive, semi-active, and active categories. Passive RFID tags derive power from the electromagnetic field and lack an internal power supply, whereas semi-active tags receive power for internal circuits and broadcasting from the reader's electromagnetic field. Active RFID tags have their power supply for both internal circuits and broadcasting, offering long-range communication and superior tracking accuracy [15-16]. Despite advancements, existing tracking algorithms, such as the Hidden Markov Model (HMM) and linear regression-based approaches, exhibit high tracking errors in indoor environments [17-18]. This motivates the need for further research to enhance tracking accuracy and reduce localization errors in RFID-based indoor tracking systems. The proposed research aims to address these challenges through a multi-faceted approach. Four key processes are formulated to achieve the overarching objective of improved tracking accuracy:

1. Signal Improvement: Mitigating RSSI signal fluctuations arising from multipath effects and interference in indoor environments.
2. Optimization-based Virtual Reference Tag Allocation: Strategically allocating virtual reference tags to optimize tracking accuracy.
3. Quantum-Based Localization: Leveraging quantum-based techniques to enhance the precision of initial target tag localization.
4. Deep Reinforcement Learning-Based Tracking: Employing deep reinforcement learning for dynamic tracking in real-time indoor environments.

Existing RFID-based tracking systems grapple with issues such as interference, signal-blocking, and low positioning accuracy. The proposed research aims to contribute to the refinement of indoor tracking systems, addressing these challenges and enhancing tracking accuracy. The subsequent sections delve into each formulated process, discussing methodologies, challenges, and potential contributions to the field. Fig. 1 represents the general RFID tracking system.

Table 1 represents the notation and description used in our proposed VIRALTRACK model.

Table 1: Notation and its description

Notation	Description
TX_p	The transmission power of the source device
RX_p	The remaining power of the wave at the receiver
RX_g	value of receiver gain
TX_g	transmitter gain
λ	wavelength
d	distance between the source and the destination
V_t	Virtual reference tag
R_t	Reference tag
r^2	Distance from the reference tag in the grid
S_{V_t}	The signal intensity of the virtual reference tag
S_{R_t}	The initial signal intensity of the reference tag
y	Distance factor
ρ	Humidity
K	Temperature
W_{V_t}	Weight value between the input layer and hidden layer
μ_t	The threshold value of $t\,th$ hidden neuron
μ_t	sigmoid function
λ	Discount factor
TRP	True positive rate
Ω	Number of identified virtual reference tag
$\int$	The total number of virtual reference tags.

This paper introduces the VIRALTRACK model, a novel RFID localization and tracking system designed for indoor environments, incorporating advanced artificial

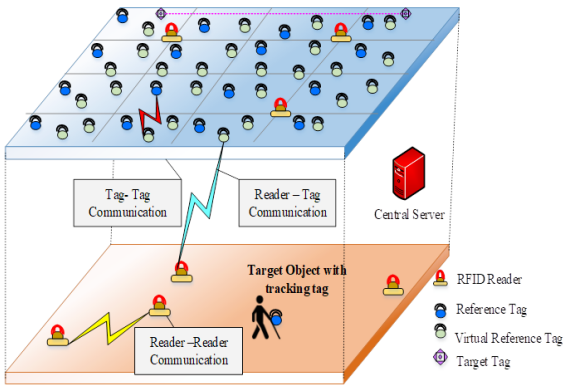

Figure 1: RFID tracking system

intelligence techniques. The key contributions of this research encompass several innovative components. Firstly, the Extended Gradient Filter (EGF) is proposed to effectively mitigate the impact of noise-induced RSSI fluctuations. Secondly, an optimization-based strategy for virtual reference tag allocation is introduced, utilizing the Emperor Penguin Colony (EPC) algorithm. This approach optimizes the number of virtual tags by considering factors such as Signal-to-Noise Ratio (SNR), tag quantity, and environmental conditions like temperature and humidity, ultimately enhancing tracking accuracy. The third contribution involves Quantum-based localization, where the position estimation is achieved through a Quantum-Inspired Neural Network (QNN). The SignRank algorithm is proposed to select the optimal virtual reference tag within specific grids, aiming to reduce errors during tracking. Lastly, deep reinforcement learning-based tracking is presented, employing the Twin Delayed Deep Deterministic Policy Gradient (TD3) algorithm. This method takes into account various parameters, including distance, phase, orientation, and previous coordinates, leading to a substantial improvement in tracking accuracy within indoor environments. The proposed VIRALTRACK method is thoroughly evaluated based on tracking accuracy, tracking error, and cumulative probability, demonstrating its effectiveness in addressing challenges associated with RFID localization and tracking in indoor settings.

2 Literature survey

In the realm of indoor object tracking for e-health applications, Radio Frequency Identification (RFID) technology has emerged as a prominent solution, as evidenced by various proposals in the literature. One such proposition by Author [21] advocates for the use of ultra-high frequency RFID to facilitate tracking and management of mobile tags within indoor environments, particularly emphasizing its application in hospitals. This system relies on signal information exchanged between RFID readers and tags, with a focus on utilizing received signal strength for precise localization of patients and medical items. Meanwhile, Author [22] proposes an indoor tracking system that integrates RFID information with Inertial Measurement Unit (IMU) data. Although the system employs the unscented Kalman filter algorithm based on Received Signal Strength Indication (RSSI) data, its limitations in non-Gaussian environments are acknowledged.

In an attempt to address challenges associated with RFID-based tracking, innovative methods are explored. Author [23] introduces a spinning antenna-based system, employing three key pieces of information—RSSI, Doppler frequency, and phase—for localization. Notably, preprocessing steps are incorporated to eliminate signal noise, enhancing the accuracy of object localization. On a different front, the work of Author [24] focuses on medical equipment tracking within indoor spaces, utilizing RFID tag information to ascertain the location of each piece of equipment. Moreover, efforts have been made to enhance indoor positioning algorithms, as seen in Author [25]'s work, which incorporates the LANDMARK algorithm and K-Nearest Neighbor (K-NN) algorithm for RFID tags. However, challenges are noted in the initial parameter selection for K-NN, which impacts the system's effectiveness in indoor positioning scenarios.

Various strategies are proposed to compensate for signal loss and improve accuracy in RFID-based tracking. Author [26] introduces a compensating signal loss-based RFID system, leveraging a filter to mitigate ambiguity in gathered information and employing a triangulation algorithm for object localization. Similarly, Author [27] integrates robust support vector regression and Kalman filter algorithms in a reference tag-supported RFID system to track moving objects, with the Kalman filter serving to eliminate RSSI fluctuations from the received signal. Despite the effectiveness of the system, concerns are raised about the time consumption of the support vector regression algorithm, impacting overall tracking accuracy. In the pursuit of efficient tracking in indoor environments, Author [28] presents a model with noise-filtering mechanisms for mobile targets. The system's design includes pre-filter and post-filter components in RFID tags to enhance the tracking process. Moreover, real-time tracking solutions utilizing passive RFID tags and low-frequency transmission are explored by Author [29], underscoring the practical deployment of four passive RFID tags on each moving object for accurate tracking within indoor environments.

The advancement of localization methods extends to the use of complex algorithms such as the particle

filter, laser ranging model, and Density-Based Spatial Clustering of Application with Noise (DBSCAN) algorithm, as proposed by Author [30]. The intricacies of tracking are further addressed by Author [31], who introduces an active RFID-based moving target prediction system. This system utilizes virtual reference tags and a linear regression model to effectively track moving objects within indoor locations. Meanwhile, the paradigm shifts in tracking strategies with device-free systems, as illustrated by Author [32], who employs the Hidden Markov Model (HMM) algorithm for trajectory estimation of moving objects. Furthermore, the paper by Author [33] introduces a differential received signal strength-based tracking system for construction equipment within indoor environments, utilizing four RFID readers and signal information from mobile target tags at different positions for precise tracking. A range-free indoor tracking algorithm is also proposed by Author [34], leveraging methods such as Framed Slotted Aloha and Tree Walking algorithms. However, concerns arise regarding the lack of noise removal in this approach, potentially affecting the accuracy of mobile object tracking. Finally, Author [35] proposes an indoor mobile target tracking solution using the multi-direction weight position Kalman filter, which integrates Gaussian weight computation and velocity estimation to remove RSSI fluctuations and noise interference, thereby enhancing overall tracking accuracy in indoor environments. These diverse approaches collectively contribute to the evolving landscape of RFID-based indoor tracking systems, each addressing specific challenges and pushing the boundaries of accuracy and efficiency in different applications.

3 Problem statement

In the realm of RFID indoor tracking, researchers grapple with persistent challenges in enhancing tracking accuracy and minimizing errors. The proposed tracking model, denoted as T_m, introduces a comprehensive approach where 'm' signifies the moving object, and 'P' designates the indoor position based on an RFID reader's specific location [36]. Existing studies reveal several issues; for instance, an optimization algorithm for unconstrained indoor tracking struggles with efficacy in the face of increased RFID tag interference. This algorithm relies solely on the distance parameter, neglecting crucial phase, location, and orientation information, thus diminishing tracking accuracy [36].

$$T_m = \{\left(m\left(P_1, P_2, \ldots, P_n\right)\right) | \left(\forall P_n\right)\left(P_n \in L_m \cdot \left(P_n.t < P_{n+1}.t_m\right)\right)\}$$

Another set of challenges arises in a semi-active RFID system that encounters difficulties due to inadequate noise removal and the dependence on triggers for signal transmission [37]. Additionally, the limitation of a single RFID reader poses challenges in effectively tracking multiple mobile targets [37]. These issues persist in data-driven approaches, like the KNN-HMM algorithm, which grapples with complexities in initial parameter selection and time consumption, ultimately diminishing tracking accuracy [38]. Similarly, passive RFID-based real-time tracking systems face particle filter-related challenges, including particle degradation and sample depletion, particularly in non-Gaussian environments [39]. Moreover, the utilization of passive RFID tags introduces constraints related to power resources and real-time tracking feasibility [39].

In a distinct approach, an indoor positioning system relying on the support vector regression algorithm contends with challenges stemming from ineffective noise removal mechanisms, reduced localization accuracy due to excessive reference tags, and prolonged processing times [40]. These collective challenges underscore the need for innovative solutions to enhance the robustness and precision of RFID-based indoor tracking systems [40].

4 Viraltrack system model

In our proposed work, we confront the pervasive challenges inherent in existing indoor mobile object tracking systems. The architecture of our devised system encompasses five pivotal components: RFID readers, real reference tags, virtual reference tags, target tags, and a centralized server. Opting for active RFID tags, we leverage their extended communication range and independence from power sources, drawing an advantage for enhanced performance. Our conceptualization adopts a 3D grid configuration, recognizing the efficacy of real-time indoor tracking within a three-dimensional spatial context. To strategically deploy our system, we position four RFID readers in the ceiling of the indoor environment, complemented by a singular real reference tag allocated to each grid. Our primary objective revolves around augmenting tracking accuracy and curbing localization errors within the indoor setting. The procedural framework of the proposed VIRALTRACK system is illustrated in Fig. 2.

The first critical process in our framework is signal improvement, where we introduce the Extended Gradient Filter (EGF) algorithm. This algorithm operates by effectively minimizing fluctuations in Received Signal Strength Indicator (RSSI), thereby enhancing signal stability and, consequently, improving tracking accuracy. The second process revolves around optimization-based virtual reference tag allocation. Here, we em-

ploy the Emperor Penguin Colony (EPC) optimization algorithm to strategically assign virtual reference tags, addressing interference issues associated with real reference tags in the RFID tracking system. By optimizing the allocation of virtual reference tags, we elevate tracking accuracy.

The third pivotal process introduces quantum-based localization, incorporating the Quantum Neural Network (QNN). This quantum-inspired approach accelerates initial position estimation, leading to optimal results in moving object localization. By leveraging quantum principles, we navigate challenges associated with conventional methods, reducing errors during the tracking process. The final process employs deep reinforcement learning-based tracking, employing the Twin Delayed Deep Deterministic Policy Gradient (TD3) algorithm. This algorithm harnesses RFID reader information to accurately track moving target tags, contributing to a comprehensive solution for increased tracking accuracy within the indoor environment.

In summary, our VIRALTRACK model integrates these four processes cohesively, culminating in a robust system that adeptly addresses the intricacies of indoor mobile object tracking, demonstrating enhanced tracking precision and reduced localization inaccuracies.

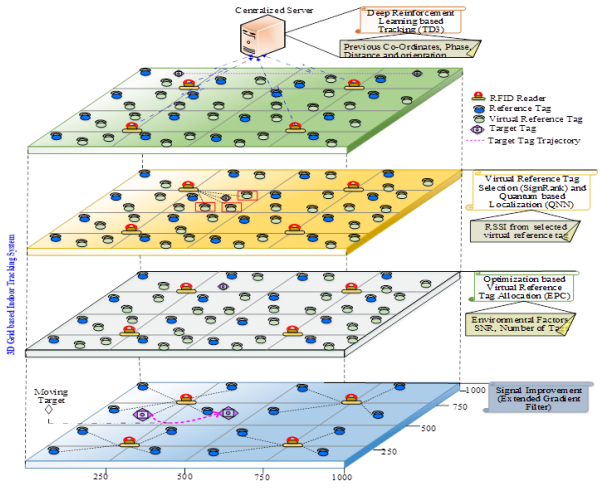

Figure 2: Proposed VIRALTRACK System model

4.1 Signal improvement

The primary process in our work is a signal improvement since the indoor environment is highly affected by the multipath effects, dead spots and interference. These issues increase the noises in the received RSSI signal. RSSI is a good indicator to predict the unknown node's current position. RSSI is an estimation of dBm, which is 10 times the logarithm of the power ratio p at the receiving end and the reference power p_r. This value is inversely proportional to the square of the distance. Hence, our work employs the EGF algorithm to effectively remove the RSSI fluctuations caused by the noise. The reason for selecting this algorithm is that it performs better in multipath conditions. Besides, it performs better than traditional algorithms such as the Kalman filter.

In addition to RSSI, we evaluate the link quality evaluator (LQI) that measures the position by beacon message transmission. The low and high-frequency ranges of RSSI and LQI can be followed: -75dBm and -25dBm for low RF and high RF and 105 for low RF, and 108 for high RF, respectively. A good measurement or estimation of RSSI is required to understand the target positions. When the distance increases, then the RSS value get decreases, and it's formulated as follows:

$$RSSI = -\left(10nlog10d + A\right) \tag{1}$$

Where n represents the constant variable for signal propagation, also called

To measure the distance between the reference tags to the RFID readers, the following distance is computed as follows,

$$Distance = \frac{\left(RSSI - A\right)/\left(10 - 10n\right) - 1}{S} \tag{2}$$

Then, measures the signal attenuation factor by the following equation,

$$N = \frac{RSSI - A}{-10\log 10\left(sd + 1\right)} \tag{3}$$

The computation of RSS is that transmission power is configured in the transmitting device *TX* and receiving distance *RX* with power. Based on the Friis Free Space Transmission Model, the RSS value decreases as the distance of the source device, which is formulated as follows,

$$RX_p = TX_p \times TX_g \times RX_g \left(\frac{\lambda}{4\pi d}\right)^2 \tag{4}$$

Where TX_p is the transmission power of the source device, RX_p is the remaining power of the wave at the receiver, RX_g is the value of receiver gain, TX_g Is the transmitter gain, λ is the wavelength, and d represents the distance between the source and the destination. Then, the RSS value is transformed into the RSSI, which describes the received power of the reference power. P_r and the absolute value of P_r Is 1? mW. The RSSI value is computed as follows,

$$RSSI = 10 * log \frac{RX_p}{RF_p} [RSSI] = dB \quad (5)$$

However, the increased received power result shows a higher value of RSSI and the relationship between the RSSI and received signal power is measured, and the distance *d* is inversely proportional to the RSSI and the ideal distribution of RX_d Is not applicable. Further, the radio signal's propagation is interfered with many influencing effects. A set of RSSI values computes a mean value of RSSI, and the few packets are required from each reference tag and RSSI over the time series is computed as follows,

$$\overline{RSSI} = \frac{1}{n} \sum_{i=0}^{i=n} RSSI_i \quad (6)$$

If the EKF is applied on the RSSI signals, the approximation is applied, i.e. $a = 0.75$ and the approach uses the large difference in RSSI values normalized. It is formulated as follows,

$$RSSIn = a \times RSSIn + (1-a) * RSSIn - 1 \quad (7)$$

The above equation means that the RSSI value corresponding to the signal strength over the distance is based on the past mean value and the currently obtained value of RSSI. Approximation technique is applied to EKF for signal quality enhancement which ranges between 0 and 1, and if the value is 0, then signal quality filtering is no performed. Otherwise, it's executed optimally. In the following, we described the filtering of RSSI signals based on the obtained values of LQI and RSSI.

The following equation performs the value of LQI-based signal smoothing,

$$normalize_{RSSI_{(LQI(t))}} = a \times RSSI_t + (1-a) \times RSSI_{t-1} \quad (8)$$

The fusion value of LQI and RSSI by the normalized RSSI can be as follows,

$$normalize_{RSSI_{(Fusion(t))}} = a \times RSSI_t + (1-a) \times RSSI_{t-1} \quad (9)$$

Finally, the proposed normalization is executed by RSSIs and LQI values of recently measured are computed, and it's executed by the following,

$$normalize_{RSSI_{(Both(t))}} = a \times RSSI_t + (1-a) \times RSSI_{t-1} \quad (10)$$

Therefore, EGF is applied by normalization of LQI and RSSI values, and it is performed in Fig. 3

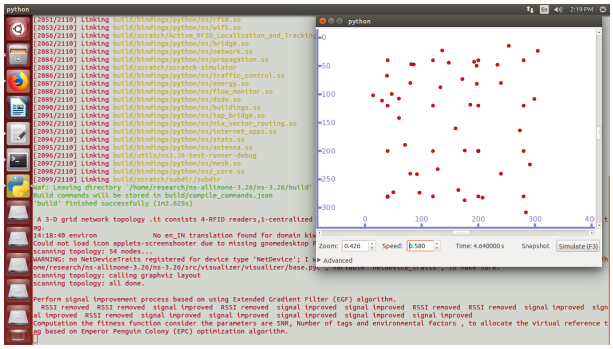

Figure 3: Conditions for Signal Quality Improvement

4.2 Optimization-based virtual reference tag allocation

Our work deploys virtual reference tags in indoor tracking to overwhelm the issues of real reference tags in the RFID tracking system. In our 3D grid network, we place one real reference tag in each grid. To reduce the interference created by the real reference tag. This is achieved by reducing the number of real reference tags via virtual reference tags. Here, the virtual reference tags are allocated by the RFID reader node placed on the ceiling of the indoor environment. It allocates several virtual reference tags by exploiting the Emperor Penguin Colony (EPC) optimization algorithm. It performs faster than traditional optimization algorithms (GWO, PSO, ACO) by obtaining results within the four iterations. It considers the succeeding parameters to compute the fitness function: SNR, number of tags and environmental factors such as temperature and humidity; these parameters are collectively termed attributes. Since these two environmental factors affect the RSSI signal in the indoor environment, based on this information, the RFID reader allocates virtual reference tags for each grid it monitors. In EPC, the optimization is based on the heat transfer and attractiveness between the penguins. Similarly, the virtual reference tags are allocated based on the attributes in our process. Initially, the position of the virtual reference tag is plotted based on the distance from the reference tag, which can be formulated as,

$$V_t = \frac{R_t}{r^2} (11)$$

Where V_t denotes the virtual reference tag, R_t denotes the reference tag and r^2 denotes the distance from the reference tag in the grid. The interference is also considered and minimized to facilitate effective communication between the tags, which can be formulated as,

$$S_{V_t} = S_{R_t} e^{-\lambda y} \quad (12)$$

Where S_{V_t} denotes the signal intensity of the virtual reference tag, S_{R_t} Denotes the initial signal intensity of

the reference tag, λ denotes the signal coefficient, and y denotes the distance factor, respectively. From this, the attractiveness G can be formulated as,

$$G = A\delta\rho K_s^4 e^{-\lambda y} \tag{13}$$

Where A denotes the surface area of the grid, δ denotes the connectivity factor, ρ denotes the humidity, and K denotes the temperature, which affects the received signals strength. The orientation of the spiral movement of the penguin is represented as,

X axis= $\eta \cos\theta e^{\mu\theta}$ (14)

Y axis= $\eta \sin\theta e^{\mu\theta}$ (15)

1. Pseudo code: EPC algorithm

```
Initialization of population of tags;
Compute tag position;
Compute signal strength (S) function;
Determine reference tag position;
For iter = 1 to Max_iter do
   Compute repeat copies of tag population;
   For i=1 to k population, do
     For j=1 to k population, do
      If S_j < S_i then
        Compute interference using eqn (12)
        Compute attractiveness using eqn (17)
        Compute spiral movement using eqn (14,15)
        Compute updation of position using eqn (19)
      End
     End
   End
Perform sorting and determine the best solution;
Update mutation factor;
Update signal coefficient;
end
```

The two points separated by a distance in the search space are calculated, which is represented as,

$$D = \int_{\theta_i}^{\theta_j} \sqrt{\eta^2\mu^2 e^{2\mu\theta} + \eta^2 e^{2\mu\theta}}\, d\theta \tag{16}$$

The multiplication of distance and attractiveness is performed to optimally allocate the position of the virtual reference tag, which can be expressed as,

The new position of the penguin is computed by adding the current position with the product of a random vector and mutation factor, which can be formulated as,

$$U_p = \left(x_P, y_P\right) + \alpha\gamma \tag{19}$$

Where α, γ denote the mutation factor and random vector, respectively. This way of allocating the virtual reference tag increases the tracking accuracy and reduces the error involved in tracking the target tag. The pseudo-code of the proposed virtual reference tag allocation is presented below.

4.3 Quantum based localization

To track the target moving tag, our work estimates its position by a localization process. For this, we execute **Quantum inspired Neural Network (QNN)** to estimate the exact position of the moving target. To find the initial position of the target tag, the RFID reader considers the RSSI signal from the nearest virtual reference tag. QNN algorithm includes quantum computation and neural networks, improving the neural network's efficiency. QNN executes based on the quantum neuron model, representing the transition relationship between the quantum states and neuron states derived from logic gates. This algorithm includes three layers input layer, hidden layer and output layer. Here RFID reader considers the RSSI signal for detecting the initial position of the target tag. RSSI signal information is considered as input, and the inputs are converted into a range value of quantum state [0,1] with range $\left[0, \frac{\pi}{2}\right]$ and the calculation of the input layer is defined as follows,

$$X_n^s = F\left(Z_n^s\right) \tag{20}$$

$$Z_n^s = \frac{\pi}{2}.Y_n \tag{21}$$

Where n represent the number of neurons and Y_n It is the nth input variable of the network, and the value of

$$x_P = \eta e^{\mu\frac{1}{\mu}ln\left\{(1-G)e^{\mu\tan^{-1}\frac{y_i}{x_i}} + Ge^{\mu\tan^{-1}\frac{y_j}{x_j}}\right\}} \cos\left\{\frac{1}{\mu}\ln\left\{(1-G)e^{\mu\tan^{-1}\frac{y_i}{x_i}} + Ge^{\mu\tan^{-1}\frac{y_j}{x_j}}\right\}\right\} \tag{17}$$

$$y_P = \eta e^{\mu\frac{1}{\mu}ln\left\{(1-G)e^{\mu\tan^{-1}\frac{y_i}{x_i}} + Ge^{\mu\tan^{-1}\frac{y_j}{x_j}}\right\}} \sin\left\{\frac{1}{\mu}\ln\left\{(1-G)e^{\mu\tan^{-1}\frac{y_i}{x_i}} + Ge^{\mu\tan^{-1}\frac{y_j}{x_j}}\right\}\right\} \tag{18}$$

$n = 1$. X_n^s Represent the input of Quantum. The second layer is a hidden layer that represents the relationship between input and output that is defined as follows,

$$X_t^h = F\left(Z_t^h\right) \tag{22}$$

$$Z_t^h = \frac{\pi}{2}.G\left(\alpha_t\right) - Arg\left(u_t^h\right) \tag{23}$$

$$u_t^h = \sum_{n=1}^{s} w_{tn}.F\left(Z_n^s\right) - F\left(\mu_t\right) = \sum_{n=1}^{s} w_{tn}.e^{i(Z_n^s)} - F(\mu_t) \tag{24}$$

$$= \sum_{n}^{s} w_{tn}.(\cos\left(Z_n^s\right) + isin\left(Z_n^s\right)) - \cos\left(\mu_t\right) - isin\left(\mu_t\right) \tag{25}$$

Where, w_{tn} Represent the weight value between the input layer and hidden layer and μ_t Represent the threshold value of *t th* hidden neuron. Substitute eqn (23) into eqn (25) and obtain z_t^h as defined as follows,

$$z_t^h = \frac{\pi}{2}.G\left(\alpha_t\right) - Arg\left(u_t^h\right) = \frac{\pi}{2}.G\left(\alpha_t\right) \tag{26}$$

$$-Arctan\left(\frac{\sum_{n=1}^{s} w_{tn}.\sin\left(Z_{n-\sin}^s\left(\mu_t\right)\right)}{\sum_{n=1}^{s} w_{tn}.\cos\left(Z_{n-\cos}^s\left(\mu_t\right)\right)}\right)$$

Where each metric belongs to the t[th] neuron in the hidden layer and the value of t=1 and μ_t Represent the sigmoid function.

The output layer provides the output for position prediction that is defined as follows,

$$Z_n = \left|Im\left(x^0\right)\right|^2 \tag{27}$$

$$x^0 = F\left(z^0\right) \tag{28}$$

$$z^0 = \frac{\pi}{2}.G\left(\alpha^0\right) - Arg\left(u^0\right) \tag{29}$$

$$u^0 = \sum_{t=1}^{T} w_t.F\left(z_t^h\right) - F\left(\mu^0\right) = \sum_{t=1}^{T} w_t.ee^{i(Z_n^s)} - F\left(\mu^0\right)(30) \tag{30}$$

$$= \sum_{m}^{M} w_t.\left(\cos\left(z_t^h\right) + isin\left(z_t^h\right)\right) - \cos\left(\mu^0\right) - isin\left(\mu^0\right) \tag{31}$$

Where, w_t Represent the weight value and μ^0 is represent the threshold value of the output neuron. Then substitute the eqn (30) into eqn (31) and obtain (μ^0) as follows,

$$z^0 = \frac{\pi}{2}.G\left(\alpha^0\right) - \arg\left(u^0\right) = \frac{\pi}{2}.G\left(\alpha^0\right) \tag{32}$$

$$-Arctan\left(\frac{\sum_{n=1}^{N} w_t.\sin\left(z_t^h\right) - \sin\left(\mu^0\right)}{\sum_{n=1}^{N} w_t.\cos\left(z_t^h\right) - \cos\left(\mu^0\right)}\right)$$

Where, z^0 represent the output which is known as the optimal position for localization. To select the optimal virtual reference tag for localization, we proposed the **SignRank** algorithm. It ranks the virtual reference tag inside each grid based on its distance. The SignRank algorithm considered the weighted graph from the QINN, and it is defined as follows,

$$G = \left(V, B^+, B^-\right) \tag{33}$$

Where the value of $B_{ij}^+ \; and B_{ij}^-$ are defined as follows,

$$B_{ij}^+ = \begin{cases} 1, \; positive link \; between \; i \; to \; j \\ 0, \; No \; positive link \; between \; i \; to \; j \end{cases} \tag{34}$$

$$B_{ij}^- = \begin{cases} 1, \; negative link \; between \; i \; to \; j \\ 0, \; No \; negative link \; between \; i \; to \; j \end{cases} \tag{35}$$

This algorithm supposes an RFID reader randomly visits the virtual references tag for localization. The RFID reader visits one neighbour's virtual reference tag, then RFID has positive and negative sign values and the high positive value is denoted as rank one; based on these rank values, the virtual reference tag is selected for localization. This value is based on the distance of the virtual reference tag.

The positive and negative value is updated every time to select the optimal virtual tag. From the ranking, it selects the optimal virtual reference tag for localization. Based on the selected RSSI signal received from the virtual reference tag and moving target tag, the RFID reader localizes the initial position of the moving target tag. This way of localizing the moving target position reduces the error during the tracking.

$$\pi^{+(a+1)} = \beta\left(\sum_{j\in IM_j^+} \pi_j^{+(a)} Q_{ij} + (1-\sigma) \sum_{\in IM_j^-} \pi_j^{-(a)} Q_{ij} + \frac{\sigma}{2M} \sum_{j=1}^{M} \pi_j^{-(a)} \right) + \frac{1-\beta}{2M} \tag{36}$$

$$\pi^{-(a+1)} = \beta\left(\sum_{j\in IM_j^-} \pi_j^{+(a)} Q_{ij} + (1-\sigma) \sum_{\in IM_j^+} \pi_j^{-(a)} Q_{ij} + \frac{\sigma}{2M} \sum_{j=1}^{M} \pi_j^{-(a)} \right) + \frac{1-\beta}{2M} \tag{37}$$

2. Pseudo code: Quantum-based localization

```
INPUT: No. of virtual reference tags {vt1, vt2, ..vtn}, d
OUTPUT: Optimal virtual reference tag
Begin
Initialize {vt1, vt2, ..vtn}, RSSI signal
{
For each virtual reference tag {vt} do
Calculate weight value for every {vt}
End for
}
Optimal position is detected for localization
Take weighted graph (G) from QINN
  For every node i in G do
    For every neighbor j of node i do
    if (Bij+ == 1) then
        Select high positive rank node and set high
        rank using eqn(34)
        Optimal virtual reference tag is selected for
        localization
    else if (Bij- == 1) then
       Put a low rank for virtual reference tag using
       eqn(35)
    End If
  End For
End For
```

4.4 Deep reinforcement learning based tracking

To track the moving target in the indoor environment, we propose the Twin Delayed Deep Deterministic Policy Gradient (TD3) algorithm, one of the deep reinforcement learning algorithms. It is executed by the centralized server using the information acquired by each reader positioned in the indoor environment. It provides better results in tracking by learning the indoor environment effectually. Besides, it outperforms existing reinforcement learning algorithms. It utilizes subsequent parameters to track the moving target: distance, phase, orientation and previous coordinates. By utilizing this information in tracking, our proposed method tracks the moving target tag effectually. The tracking of moving tags is modelled as a Markov Decision Process (MDP), which comprises attributes, namely state (*S*), action (Å), reward (ℝ) and discount factor (ג). The state represents the state space of the system at a time (*τ*) upon which an action is performed by the agent. Depending on the action, the system receives a reward for each time step. The discount factor denotes the acceptance of current rewards over upcoming ones. The pol-

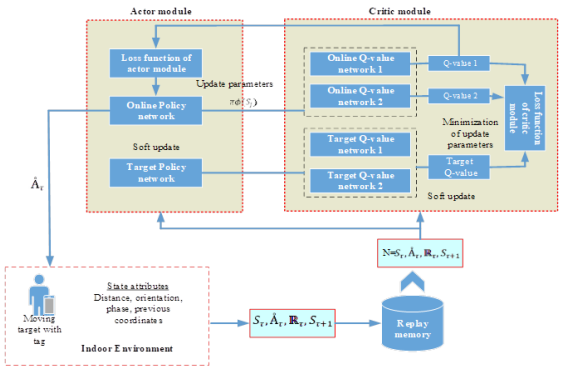

Figure 4a: Process of deep reinforcement learning-based tracking

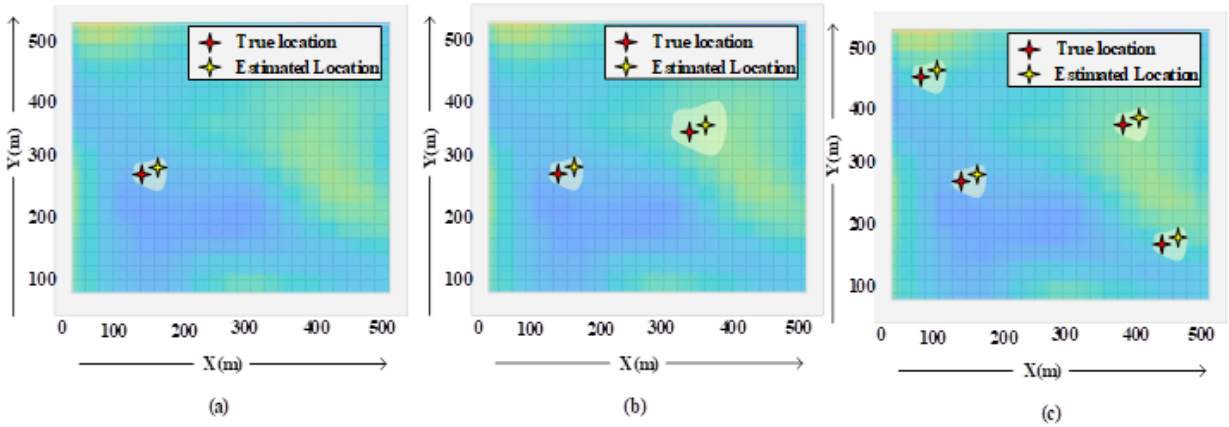

Figure 4b: a) One target b) Two target c) Multi target

icy refers to the selection of action by the agent, and an optimal policy is termed the policy of the agent, which achieves expected returns. In our tracking process, the state is defined as the current position of the moving target tag, which includes the attributes. The process of deep reinforcement learning-based tracking is represented in Fig. 4a, and Fig 4b represents the tracking position of the moving object, 4b.a represent one moving target, 4b.b represent two targets and 4b.c represent multi-target.

The action carried out by the DRL agent is tracking the location based on state attributes. The reward is generated based on how well the agent tracks the target tag. The implementation of tracking is formulated as,

$$Q(S,\text{Å}) = E_{\pi(s)}[\mathbb{R}_{\tau+1} + \\ +\lambda Q(S_{\tau+1},\text{Å}_{\tau+1}) \mid S_\tau = S,\text{Å}_\tau = \text{Å} \quad (38)$$

The value function on following the policy π (s) is termed as the expected return, which can be formulated as,

$$V_\pi(s) = \sum_{a\in\text{Å}} \pi(\mid \text{Å}\, S) Q_\pi(S,\text{Å}) \quad (39)$$

The actor module performs actions based on the current state attributes. The actor module is trained accordingly to achieve the optimal policy. The loss obtained in the actor module is formulated as,

$$l_A = E[Q_{\theta 1}(S,\text{Å})|_{S=S_j\text{Å},=\pi\phi(S_j)}] \quad (40)$$

Where ϕ and $\Theta 1$ represent the parameters of the online poly network and online Q value network, the critic module is incorporated to evaluate the actions taken by the actor module to achieve the optimal policy. The critic produces the Q value, which is improved by updating the network parameters. The optimal Q-value function is represented as,

$$x_j = \mathbb{R}(S_j,\text{Å}_j) + \lambda min_{i=1,2} Q_{\hat{\theta}i}(S_{j+1}, \pi\phi'(S_{j+1})) \quad (41)$$

Where, $\hat{\theta}i$ and ϕ' Denotes the network parameters of the target Q-value network and target policy network. The reward that the agent can receive by taking an action Å_j in the state S_j is denoted as $\mathbb{R}(S_j, \text{Å}_j)$. The loss function of the critic module can be formulated as,

$$l_C = \frac{1}{N}\sum_{j=1,2}^{N}\sum_{i=1,2}\left(x_j - Q_{\theta i}(S_j,\text{Å}_j)\right)^2 \quad (42)$$

The soft update is carried out to update target neural network parameters. Similarly, the minimization of the loss function l_C and maximization of the loss function l_A It is carried out to perform the updation of online Q-value parameters and online policy network parameters, respectively. The updation processes can be formulated as,

$$\begin{cases} \phi' \leftarrow t\phi + (1-t)\phi' \\ \hat{\theta}i \leftarrow t\hat{\theta}i + (1-t)\hat{\theta}i \end{cases} \quad (43)$$

This facilitates the agent to achieve optimal policy. Thus improves the tracking accuracy in the indoor environment.

V. Experimental study

The performance of the proposed VIRALTRACK model is evaluated, and simulation results are discussed. This section includes three subsections: simulation setup, comparative analysis and research summary.

4.5 Simulation setup

We design a 3-D grid network topology that includes four RFID readers, one centralized server, sixteen real/phy reference tags, thirty-two virtual reference tags, and one target tag. The proposed VIRALTRACK model is experimented with in 300 x 400 m simulation environment for RFID localization and tracking using intellectual techniques in the indoor environment. The simulation parameters are shown in Table 3. The system configurations are illustrated in Table 2.

Table 2: System specifications

Hardware Specification	Hard Disk	500GB
	RAM	4GB
	Network Simulator	NS3.26
Software Specification	Operating System	Ubuntu 14.04 LTS

Table 3: Simulation parameters

Parameters	Value
Network Parameters	
Area of simulation	300 × 400m
Topology	3D Grid network
RFID reader	4
Centralized server	1
Real/Phy reference tag	16
Virtual reference tag	32
Target tag	1
Channel frequency	915MHz
Fading	No

Inference of Inter channel	No
Data rate	2 Mbps
SNR-based signal reception	10
The transmission power of RFID	-45 dBm
Read range	1.62 m
Range of sensing	5.4 m
Range of inference	7.1m
Number of nodes	50
Control channel frequency	930 MHz
Radio Rx Sensitivity	-91 dBm
Sensitivity reader power	-70dBm
Sensitivity tag power	-17dBm
Transmission range	30m

Fig 5 represents the simulation environment of the proposed VIRALTRACK model, which considers the 3D grid topology. The proposed VIRALTRACK environment includes four RFID readers, one centralized server, 16 real/phy reference tags, thirty-two virtual reference tags, and one target tag.

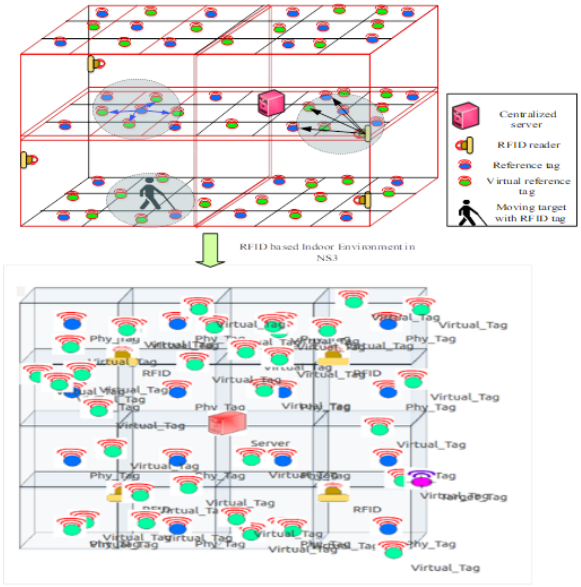

Figure 5: Simulation Environment of proposed VIRALTRACK model

And moving target with an RFID tag is also represented in the Fig. RFID readers have small coverage covering the number of virtual and reference tags. RFID reader is used to track the reference tags in an indoor environment.

Fig. 6 represents the target tag tracking process using the TD3 algorithm, performed by the centralized server by each reader positioned in the indoor environment. TD3 algorithm automatically learns the indoor environment and provides better tracking results, improving tracking accuracy.

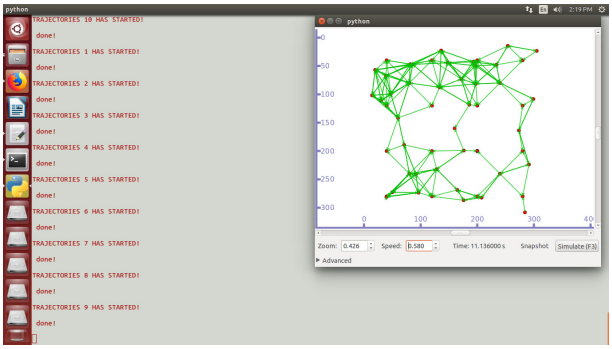

Figure 6: Target tag tracking process using TD3 algorithm

4.6 Use case

Indoor localization using RFID tags is predominantly used in smart home applications. The user's location information is gathered to make precise decisions in many cases. The advantages of RFID systems, such as non-LOS readability, contactless communication, increased data rate and security, have enabled its use in smart home applications. Further, the location information of users in the smart home facilitates the indoor navigation of elder age and visually impaired users.

Figure 7: Case diagram for an indoor scenario

Fig.7 depicts the use case diagram of RFID in the smart home in which the RFID reader is placed in the living room, which is responsible for tracking the location with the help of tags. The reference and virtual tags are placed in each room to transmit and receive radio signals with the moving target. For instance, the tags R1 to R4 are placed in the living room, R5 is placed in the portico, R6 and R7 are placed in the bedroom, R8 in the toilet, R9 in the Pooja room, R10 and R11 in the dining room, R12 in the store room and R13 in kitchen.

Table 4: RFID specifications

RFID model	RC522
Type	Active RFID
Frequency	902-928 MHz
Power source	External source
Read rate	400 tags/sec
Read range	4 to 7 meters
Memory size	64 to 2052 bits
Transmission speed	19300 bps
Temperature operated	-25° C to 55° C
Communication standard	USB
Output power	0.70mW

The specifications of the RFID communication are presented in Table 4. The signals acquired from the moving target are initially improved by using EGF to remove the fluctuations. Further, the placement of virtual tags in the 3D indoor environment by implementing EPC, which considers SNR, temperature and humidity for optimal solution. The tracking error is reduced by performing the initial localization of the moving target using the QNN model. Finally, the accurate tracking of the moving targets is performed by the centralized server using TD3.

4.7. Comparative analysis

This section evaluates the performance of the proposed VIRALTRACK model in terms of several performance metrics, such as tracking accuracy, tracking error and cumulative probability. From these performance metrics, we proved that our model work is better than existing models. The comparison analysis performs with the PSO-TRACK [36], MOIT [37] and proposed VIRALTRACK model.

4.7.1 Impact of tracking accuracy

This metric is used to evaluate the correctness of the proposed VIRALTRACK model. Tracking accuracy is calculated concerning the number of tags. Fig 8 compares tracking accuracy for both proposed and existing models. The comparison result shows that the proposed VIRALTRACK achieves high accuracy compared to other methods. And we proposed Extended Gradient Filter (EGF) to remove noise and RSSI fluctuations, increasing the tracking accuracy. In our method, we proposed optimization-based virtual tag allocation, which is used to optimize the virtual reference tag by considering SNR, many factors that affect the RSSI signal. Based on these factors, the RFID reader allocated the virtual tags that increase the tracking accuracy. And also, the proposed work performs Quantum based localization which selects the optimal virtual reference tag for localization. The optimal localization method increases the tracking accuracy and reduces the error during tracking. We proposed deep reinforcement learning-based tracking that learns the indoor environment and provides better tracking results, increasing tracking accuracy. The existing method does not perform optimal localization and tracking, which reduces tracking accuracy. The proposed VIRALTRACK method achieves 20% high accuracy than the MOIT method and 11% higher than the PSO-TRACK method.

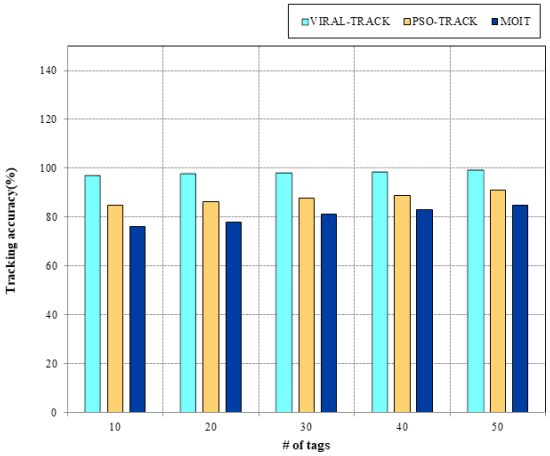

Figure 8: Tracking Accuracy vs. No. of Tags

Table 5 illustrates the numerical analysis of tracking accuracy concerning the number of tags. The table presents the average value of tracking accuracy. From the numerical analysis, the proposed VIRALTRACK model achieves high accuracy compared to others.

Table 5: *Tracking accuracy (%) analysis*

Method	# of tags
VIRAL-TRACK	98.02 ± 0.5
PSO-TRACK	87.82 ± 1.0
MOIT	80.6 ± 1.5

4.7.2 Impact of tracking error

This metric evaluates the errors during tracking due to random localization, noise, and multipath effects in an indoor environment. If the tracking error is high, the system will achieve poor accuracy. The tracking error is calculated concerning SNR, number of tags and trajectories.

Fig 9a compares tracking error for proposed and existing models for several tags. The comparison result shows that the proposed VIRALTRACK model achieves low tracking error compared to existing models. Because our proposed work performs optimal virtual reference tag allocation, which is used to reduce the interference created by the real reference tag. The virtual

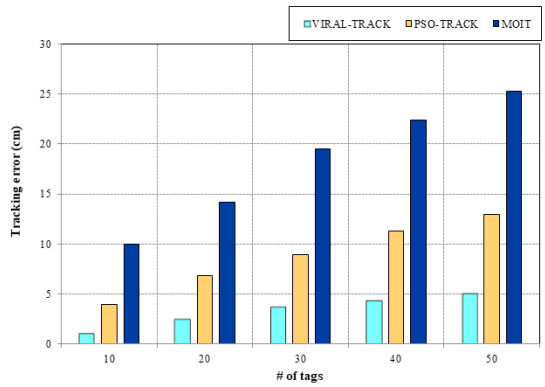

Figure 9a: Tracking error vs. No. of tags

reference tag is allocated by using Emperor Penguin Colony (EPC) algorithm, which optimally allocates the virtual reference tag, reducing tracking errors.

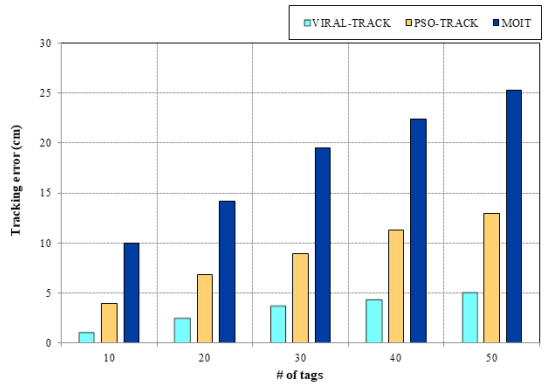

Figure 9b: Tracking Error vs. No. of trajectories

Then we perform Quantum based localization, which selects the optimal virtual reference tag localization, reducing tracking errors. To reduce tracking error, we proposed a deep reinforcement learning algorithm that learns the indoor environment automatically and takes action based on the current status of the environment, which reduces tracking error and increases tracking accuracy. The proposed VIRALTRACK model reduces by 15 cm lower than the MIOT model and 13cm lower than the PSO-TRACK model for the number of tags. Similarly, Fig 9b represents the comparison of tracking error for the number of trajectories. The result shows that the proposed VIRALTRACK model achieves less tracking error than the existing model by performing optimal localization and deep reinforcement-based tracking. The proposed VIRALTRACK reduces 18cm less than the MIOT model and 14cm less than the PSO-TRACK method.

Fig 9c represents the comparison of tracking error for SNR. The Fig. clearly states that the proposed VIRALTRACK model achieves less tracking error compared to the existing model by reducing the fluctuations of RSSI

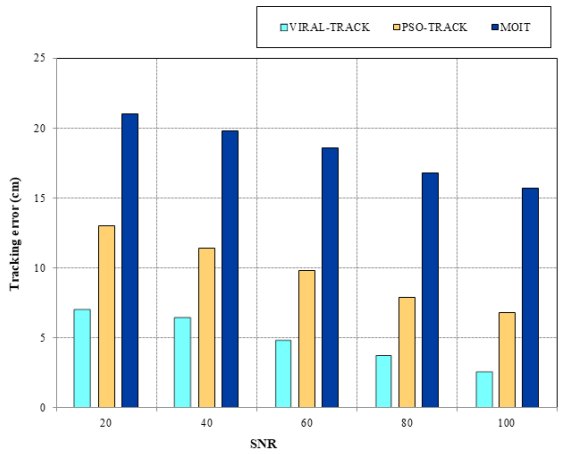

Figure 9c: Tracking Error Vs. SNR

signal using the Extended Gradient Filter (EGF), which increases single strength and reduces tracking error. And the optimal virtual tag allocation considers the SNR for calculating fitness value, thus reducing tracking errors. The proposed VIRALTRACK method achieves 13cm less than the MIOT model and 9cm less than the PSO-TRACK model. Table 6 illustrates the numerical analysis of tracking error, which shows the average value of tracking error for SNR, No. of tags and No of trajectories. From the numerical analysis, the proposed model achieves less tracking error than an existing model.

Table 6:*Tracking error (cm) analysis*

Method	SNR	# of tags	#of trajectories
VIRAL-TRACK	4.9 ± 0.05	3.8 ± 0.05	4.46 ± 0.05
PSO-TRACK	9.78 ± 0.10	8.8 ± 0.10	8.52 ± 0.10
MIOT	18.38 ± 0.15	18.28 ± 0.15	22.42 ± 0.15

4.7.3 Impact of cumulative probability

This metric is used to evaluate the cumulative probability during tracking. It is calculated based on the target positioning of the RFID tag. And also it refers to the probability that measures the odds of two or more events happenings during RFID localization and tracking in an indoor environment. Fig 10 represents the comparison of the cumulative probability of proposed and existing methods for SNR. The Fig. shows that the proposed VIRALTRACK model achieves high cumulative probability compared to existing works because our work achieves high probability for all four processes of RFID localization and tracking using intellectual techniques in an indoor environment. First, we proposed EGF to remove RSSI fluctuations, thus increasing tracking accuracy, which increases the probability value of signal power. Second, we proposed optimization-

based virtual reference tag allocation, thus increasing the allocation probability of virtual reference tags by reducing the tracking error. And third, we proposed Quantum based localization, thus increasing localization accuracy and probability. Finally, we proposed deep reinforcement learning-based tracking, which reduces tracking error and increases tracking accuracy and probability. And the cumulative probability is calculated by adding the four process probability values. The four processes achieve high probability, and then the cumulative probability also achieves high probability compared to existing models.

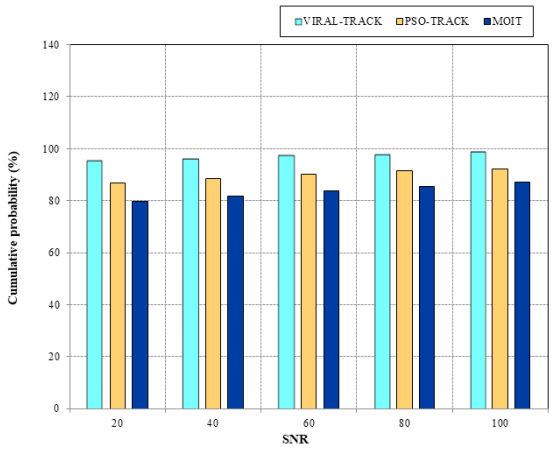

Figure 10: Cumulative Probability vs. SNR

Table 7 represents the numerical analysis of cumulative probability for SNR. The table illustrates the average value of cumulative probability. From the analysis, the proposed VIRALTRACK model achieves 14% higher than the MOIT model and 8% higher than the PSO-TRACK model.

Table 7. *Cumulative probability (%) analysis*

Method	# of tags
VIRAL-TRACK	97.08 ± 0.5
PSO-TRACK	89.76 ± 1.0
MOST	83.6 ± 1.5

4.7.4 Impact of true positive rate

This metric is used to calculate the accuracy of the RFID tracking system. TRP represent the proportion of the number of correctly identified virtual reference tag to the total number of virtual reference tag. It is calculated as follows,

$$TRP = \frac{\mathfrak{Q}}{\int} \tag{44}$$

Where TRP represents the true positive rate, $\mathfrak{Q}$ represents the number of identified virtual reference tag and $\int$ represents the total number of virtual reference tags.

Fig 11 compares the true positive rate for the proposed and existing models for motion speed. The Fig. clearly states that the proposed VIRALTRACK model achieves a high true positive rate compared to an existing model. In our method, we reduce RSSI fluctuations, improving signal strength and tracking accuracy. And also, deploy the virtual reference tags in indoor tracking, which reduces the interference created by the real reference tag, thus increasing tracking accuracy and true positive rate. QINN-based localization is performed to detect the initial position of the target tag. Then reinforcement learning-based tracking is performed to increase tracking accuracy, thus also increasing the true positive rate. In this way, we accurately track moving objects in an indoor environment, thus increasing the true positive rate.

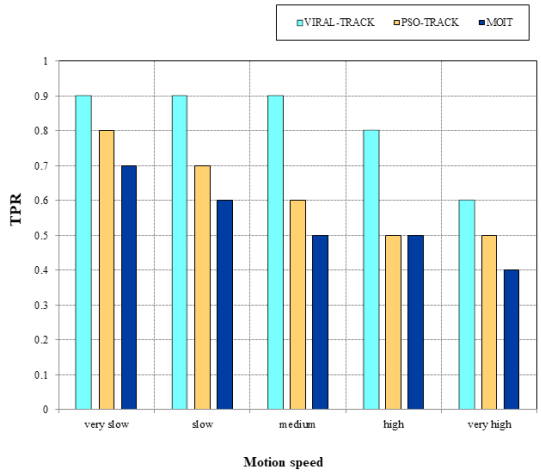

Figure 11a: True Positive Rate vs. Motion speed

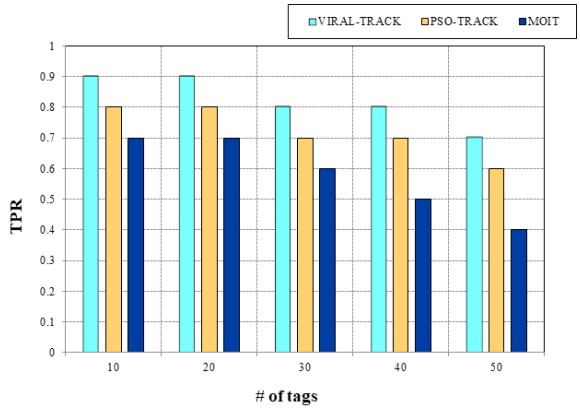

Figure 11b: True Positive Rate vs. Number of tags

Similarly, Fig. 11b represents the comparison of the true positive rate for both the proposed and existing model for some tags. The Fig. shows that the proposed VIRALTRACK model achieves a high true positive rate. The value of the true positive rate is increased exponentially with the increasing number of tags. The proposed VIRALTRACK achieves a high true positive rate by

performing signal improvement, optimization-based virtual reference tag allocation, Quantum-based localization, and deep reinforcement learning-based tracking, which increases the true positive rate.

Table 8: *True positive rate analysis*

Method	Motion speed	# of tags
VIRAL-TRACK	0.82 ± 0.001	0.82 ± 0.001
PSO-TRACK	0.62 ± 0.005	0.72 ± 0.005
MIOT	0.54 ± 0.015	0.58 ± 0.015

Table 8 represents the numerical analysis of the true positive rate for motion speed and number of tags for both the proposed and existing models. The table illustrates the average value of the true positive rate. From the numerical analysis, the proposed VIRALTRACK achieves a high true positive rate.

The VIRALTRACK model presented in this study demonstrates superior performance compared to existing Radio Frequency Identification (RFID) localization and tracking models in indoor environments. The Extended Gradient Filter enhances received signals, significantly boosting tracking accuracy. An optimization-based virtual reference tag allocation minimizes interference from multiple real reference tags, further refining system performance. Quantum Neural Network-based Localization accelerates initial position estimation, providing optimal results in moving object localization. The Tracking and Detection Dimensional Deep Deterministic Policy Gradients (TD3)-based learning algorithm ensures accurate tracking of moving targets by leveraging RFID reader information. Through signal improvement, optimized tag allocation, quantum-inspired techniques, and deep reinforcement learning, the VIRALTRACK model represents a notable advancement in RFID-based localization and tracking, promising enhanced accuracy and adaptability in dynamic indoor settings.

5 Conclusion

This paper proposes VIRALTRACK, a novel system designed for Radio Frequency Identification (RFID) localization and tracking within indoor environments. The primary objective is to enhance tracking accuracy and minimize errors during the tracking process. An innovative Extended Gradient Filter (EGF) algorithm is proposed to refine signal strength by reducing Received Signal Strength Indication (RSSI) fluctuations. The deployment of virtual reference tags, managed by the Emperor Penguin Colony (EPC) optimization algorithm, addresses challenges associated with real reference tags in RFID tracking systems, ultimately augmenting tracking accuracy. The subsequent step involves target moving tag localization, employing a Quantum-inspired Neural Network (QNN) for precise position estimation and error reduction during tracking. The final stage incorporates a deep reinforcement learning-based tracking mechanism utilizing the Twin Delayed Deep Deterministic Policy Gradient (TD3). This comprehensive approach significantly enhances tracking accuracy within the specified environment. The VIRALTRACK model's performance is evaluated based on tracking accuracy, tracking error, and cumulative probability, positioning it as a promising advancement in RFID-based localization and tracking. Future work aims to address the impact of moving target shadows on RSSI signal quality and explore multi-target localization to further enhance overall efficiency.

6 Conflicts of interests

The authors have no Conflicts of interests/Competing interests to disclose.

7 References

1. Zhang, Y., Gong, X., Liu, K., & Zhang, S. (2021). Localization and Tracking of an Indoor Autonomous Vehicle Based on the Phase Difference of Passive UHF RFID Signals. *Sensors (Basel, Switzerland), 21*. https://doi.org/10.3390/s21093286
2. Liu, M., Wang, H., Yang, Y., Zhang, Y., Ma, L., & Wang, N. (2019). RFID 3-D Indoor Localization for Tag and Tag-Free Target Based on Interference. *IEEE Transactions on Instrumentation and Measurement, 68*, 3718-3732. https://doi.org/10.1109/TIM.2018.2879678
3. Bernardini, F., Buffi, A., Fontanelli, D., Macii, D., Magnago, V., Marracci, M., Motroni, A., Nepa, P., & Tellini, B. (2021). Robot-Based Indoor Positioning of UHF-RFID Tags: The SAR Method With Multiple Trajectories. *IEEE Transactions on Instrumentation and Measurement, 70*, 1-15. https://doi.org/10.1109/TIM.2020.3033728
4. Tao, B., Haibing, W., Gong, Z., Yin, Z., & Ding, H. (2020). An RFID-Based Mobile Robot Localization Method Combining Phase Difference and Readability. *IEEE Transactions on Automation Science and Engineering*, 1-11. https://doi.org/10.1109/TASE.2020.3006724
5. Bernardini, F., Buffi, A., Motroni, A., Nepa, P., Tellini, B., Tripicchio, P., & Unetti, M. (2020). Particle Swarm Optimization in SAR-Based Method Enabling Real-Time 3D Positioning of UHF-RFID

Tags. *IEEE Journal of Radio Frequency Identification, 4*, 300-313. https://doi.org/10.1109/JRFID.2020.3005351
6. Ma, Y., Tian, C., & Jiang, Y. (2019). A Multitag Cooperative Localization Algorithm Based on Weighted Multidimensional Scaling for Passive UHF RFID. *IEEE Internet of Things Journal, 6*, 6548-6555. https://doi.org/10.1109/JIOT.2019.2907771
7. Wang, X., Wang, X., Mao, S., Zhang, J., Periaswamy, S.C., & Patton, J. (2020). Indoor Radio Map Construction and Localization With Deep Gaussian Processes. *IEEE Internet of Things Journal, 7*, 11238-11249. https://doi.org/10.1109/JIOT.2020.2996564
8. Paolini, G., Masotti, D., Antoniazzi, F., Cinotti, T.S., & Costanzo, A. (2019). Fall Detection and 3-D Indoor Localization by a Custom RFID Reader Embedded in a Smart e-Health Platform. *IEEE Transactions on Microwave Theory and Techniques, 67*, 5329-5339. https://doi.org/10.1109/TMTT.2019.2939807
9. Lai, J., Luo, C., Wu, J., Li, J., Wang, J., Chen, J., Feng, G., & Song, H. (2020). TagSort: Accurate Relative Localization Exploring RFID Phase Spectrum Matching for Internet of Things. *IEEE Internet of Things Journal, 7*, 389-399 . https://doi.org/10.1109/JIOT.2019.2950174
10. Wang, P., Guo, B., Wang, Z., & Yu, Z. (2020). ShopSense:Customer Localization in Multi-person Scenario with Passive RFID Tags. *IEEE Transactions on Mobile Computing*, 1-1. https://doi.org/10.1109/TMC.2020.3029833
11. Li, C., Tanghe, E., Plets, D., Suanet, P., Hoebeke, J., Poorter, E.D., & Joseph, W. (2020). ReLoc: Hybrid RSSI- and Phase-Based Relative UHF-RFID Tag Localization With COTS Devices. *IEEE Transactions on Instrumentation and Measurement, 69*, 8613-8627. https://doi.org/10.1109/TIM.2020.2991564
12. Ma, Y., Tian, C., & Liu, H. (2020). MUSE: A Multistage Assembling Algorithm for Simultaneous Localization of Large-Scale Massive Passive RFIDs. *IEEE Transactions on Mobile Computing*. https://doi.org/10.1109/TMC.2020.3030039
13. Ma, Y., Zhang, Y., Wang, B., & Ning, W. (2021). SCLA-RTI: A Novel Device-Free Multi-Target Localization Method Based on Link Analysis in Passive UHF RFID Environment. *IEEE Sensors Journal, 21*, 3879-3887. https://doi.org/10.1109/JSEN.2020.3023096
14. Magnago, V., Palopoli, L., Buffi, A., Tellini, B., Motroni, A., Nepa, P., Macii, D., & Fontanelli, D. (2020). Ranging-Free UHF-RFID Robot Positioning Through Phase Measurements of Passive Tags. *IEEE Transactions on Instrumentation and Measurement, 69*, 2408-2418. https://doi.org/10.1109/TIM.2019.2960900
15. Scherhäufl, M., Rudić, B., Stelzer, A., & Pichler-Scheder, M. (2019). A Blind Calibration Method for Phase-of-Arrival-Based Localization of Passive UHF RFID Transponders. *IEEE Transactions on Instrumentation and Measurement, 68*, 261-268. https://doi.org/10.1109/TIM.2018.2834078
16. Woensel, W.V., Roy, P., & Abidi, S. (2020). Indoor location identification of patients for directing virtual care: An AI approach using machine learning and knowledge-based methods. *Artificial intelligence in medicine, 108*, 101931 . https://doi.org/10.1016/j.artmed.2020.101931
17. Alshamaa, D., Chkeir, A., Mourad, F., & Honeine, P. (2019). A Hidden Markov Model for Indoor Trajectory Tracking of Elderly People. *2019 IEEE Sensors Applications Symposium (SAS)*, 1-6. https://doi.org/10.1109/SAS.2019.8706002
18. Park, J., Kim, Y., & Lee, B.K. (2020). Passive Radio-Frequency Identification Tag-Based Indoor Localization in Multi-Stacking Racks for Warehousing. *Applied Sciences, 10*, 3623. https://doi.org/10.3390/app10103623
19. Shen, L., Zhang, Q., Pang, J., Xu, H., Li, P., & Xue, D. (2019). ANTspin: Efficient Absolute Localization Method of RFID Tags via Spinning Antenna. *Sensors (Basel, Switzerland), 19*. https://doi.org/10.3390/s19092194
20. López, Y.Á., Franssen, J., Narciandi, G.Á., Pagnozzi, J., Arrillaga, I.G., & Andrés, F.L. (2018). RFID Technology for Management and Tracking: e-Health Applications. Sensors. https://doi.org/10.3390/s18082663.
21. Wang, F., Su, T., Jin, X., Zheng, Y., Kong, J., & Bai, Y. (2018). Indoor Tracking by RFID Fusion with IMU Data. 21 (4), 1768-1777. https://doi.org/10.1002/asjc.1954
21. Tsai, M.-H., Pan, C.-S., Wang, C.-W., Chen, J.-M., & Kuo, C.-B. (2018). RFID Medical Equipment Tracking System Based on a Location-Based Service Technique. Journal of Medical and Biological Engineering, 39, 163-169. https://doi.org/10.1007/s40846-018-0446-2
22. Cui, D., & Zhang, Q. (2019). The RFID data clustering algorithm for improving indoor network positioning based on LANDMARC technology. Cluster Computing. 22, 5731–5738. https://doi.org/10.1007/s10586-017-1485-0
23. Modeer, M.R., Vette, S., & Engell, S. (2019). Compensating Signal Loss in RFID-Based Localization Systems. 52 (8), 142-147. https://doi.org/10.1016/j.ifacol.2019.08.062
24. Chai, J., Wu, C., Zhao, C., Chi, H.-L., Wang, X., Ling, B. W.-K., & Teo, K. L. (2017). Reference tag supported RFID tracking using robust support vector regression and Kalman filter. Advanced Engineering Informatics, 32, 1–10. https://doi.org/10.1016/j.aei.2016.11.002

25. Bergeron, F., Bouchard, K., Gaboury, S., & Giroux, S. (2018). Tracking objects within a smart home. Expert Systems with Applications, 113, 428–442. https://doi.org/10.1016/j.eswa.2018.07.009
26. Ramudzuli, Z. R., Malekian, R., & Ye, N. (2017). Design of a RFID System for Real-Time Tracking of Laboratory Animals. Wireless Personal Communications, 95(4), 3883–3903. https://doi.org/10.1007/s11277-017-4030-9
27. Ur Rehman, S., Liu, R., Zhang, H., Liang, G., Fu, Y., & Qayoom, A. (2019). Localization of Moving Objects Based on RFID Tag Array and Laser Ranging Information. Electronics, 8(8), 887. https://doi.org/10.3390/electronics8080887
28. Baha Aldin, N., Erçelebi, E., & Aykaç, M. (2017). An Accurate Indoor RSSI Localization Algorithm Based on Active RFID System with Reference Tags. Wireless Personal Communications, 97(3), 3811–3829. https://doi.org/10.1007/s11277-017-4700-7
29. Li, L., Guo, C., Liu, Y., Zhang, L., Qi, X., Ren, Y., … Chen, F. (2018). Accurate Device-Free Tracking Using Inexpensive RFIDs. Sensors, 18(9), 2816. https://doi.org/10.3390/s18092816
30. Wu, C., Wang, X., Chen, M., & Kim, M. J. (2019). Differential received signal strength based RFID positioning for construction equipment tracking. Advanced Engineering Informatics, 42, 100960. https://doi.org/10.1016/j.aei.2019.100960
31. Seol, S., Lee, E.-K., & Kim, W. (2017). Indoor mobile object tracking using RFID. Future Generation Computer Systems, 76, 443–451. https://doi.org/10.1016/j.future.2016.08.005
32. Zhu, D., Zhao, B., & Wang, S. (2018). Mobile target indoor tracking based on Multi-Direction Weight Position Kalman Filter. Computer Networks, 141, 115–127. https://doi.org/10.1016/j.comnet.2018.05.021
33. Li, J., Feng, G.N., Wei, W., Luo, C., Cheng, L., Wang, H., Song, H., & Ming, Z. (2018). PSOTrack: A RFID-Based System for Random Moving Objects Tracking in Unconstrained Indoor Environment. IEEE Internet of Things Journal, 5, 4632-4641. https://doi.org/10.1109/JIOT.2018.2795893
34. Kong, H., & Yu, B. (2018). A Moving Object Indoor Tracking Model Based on Semiactive RFID., 2018, 1-8. https://doi.org/10.1155/2018/4812057
35. Ruan, W., Sheng, Q. Z., Yao, L., Li, X., Falkner, N. J. G., & Yang, L. (2018). Device-free human Localization and tracking with UHF passive RFID tags: A data-driven approach. Journal of Network and Computer Applications, 104, 78–96. https://doi.org/10.1016/j.jnca.2017.12.010
36. Zhao, R., Zhang, Q., Li, D., Chen, H., & Wang, D.Q. (2018). PRTS: A Passive RFID Real-Time Tracking System Under the Conditions of Sparse Measurements. IEEE Sensors Journal, 18, 2097-2106. https://doi.org/10.1109/JSEN.2018.2789350
37. Xu, H., Wu, M., Li, P., Zhu, F., & Wang, R. (2018). An RFID Indoor Positioning Algorithm Based on Support Vector Regression. Sensors, 18(5). https://doi.org/10.3390/s18051504

Copyright © 2023 by the Authors. This is an open access article distributed under the Creative Commons Attribution (CC BY) License (https://creativecommons.org/licenses/by/4.0/), which permits unrestricted use, distribution, and reproduction in any medium, provided the original work is properly cited.

Arrived: 24. 07. 2023
Accepted: 02. 02. 2024

Original scientific paper
https://doi.org/10.33180/InfMIDEM2023.402

Informacije MIDEM
Journal of Microelectronics,
Electronic Components and Materials
Vol. 53, No. 4(2023), 225 – 231

Polypropylen Carbonate Based Temporary Bonding/ Debonding Triggered by Microwave

Qiuping Yang[1,2,3], Zhe Lin[4] and Zhiyuan Zhu[1]

[1]College of Electronic Engineering, Southwest University, Chongqing, China
[2]National Key Laboratory of Materials for Integrated Circuits, Shanghai Institute of Microsystem and Information Technology, Chinese Academy of Sciences, Shanghai, China
[3]Hubei Key Laboratory of Electronic Manufacturing and Packaging Integration, Wuhan University, Wuhan, China
[4]Ocean College, Zhejiang University, China

Abstract: This paper addresses the issues that are prone to occur in the process of thinning and polishing ultra-thin wafers, such as deformation, fragmentation, damage, etc. A study was conducted on a photoacid generator (PAG) and graphite powder (C) as a load for polypropylene carbonate (PPC), utilizing microwave heating for bonding layers to achieve a rapid, efficient, and convenient temporary bonding solution. For the (PPC+PAG+C) bonding structure, the highest average shear strength reached 5.1 MPa. During the debonding process, microwave heating of the graphite powder transfers heat to the bonding layer, causing the acid generator within the bonding layer to decompose, facilitating rapid and convenient debonding.

Keywords: temporary bonding; debonding; wafers; Polypropylene carbonate (PPC); microwave

Mikrovalovno prožena začasna vez / ločevanje na osnovi polipropilen karbonata

Izvleček: Članek obravnava težave, ki se lahko pojavijo v procesu tanjšanja in poliranja ultra tankih rezin, kot so deformacije, drobljenje, poškodbe itd. Izvedena je bila študija fotokislinskega generatorja (PAG) in grafitnega prahu (C) kot obremenitvi za polipropilen karbonat (PPC) z uporabo mikrovalovnega segrevanja veznih plasti, da bi dosegli hitro, učinkovito in priročno rešitev za začasno spajanje. Pri strukturi spajanja (PPC+PAG+C) je najvišja povprečna strižna trdnost dosegla 5,1 MPa. Med postopkom ločevanja se z mikrovalovnim segrevanjem grafitnega prahu prenaša toplota na vezni sloj, zaradi česar generator kisline v vezivnem sloju razpade, kar omogoča hitro in priročno ločevanje.

Ključne besede: začasno spajanje; ločevanje; Rezine; polipropilen karbonat (PPC); mikrovalovna pečica

** Corresponding Author's e-mail: zyuanzhu@swu.edu.cn*

1 Introduction

Technological advancements are approaching the physical limits of chip size, rendering traditional horizontal integration based on Moore's Law inadequate. By 2020, technology nodes had shrunk to a few nanometers [1]. With the development of three-dimensional integration, it is widely believed to supplement the current Moore's Law. Vertical integration technology is currently being actively developed [2]. The main advantages of 3D integration are not only the small size of IC chips, but also the ability to achieve high-density serial interconnects and low power consumption, which is difficult to achieve with traditional 2D-LSI methods [3]. 3D integration can be achieved through chip-to-chip stacking [4], chip-to-wafer stacking [5,6], or wafer-to-wafer stacking [7,8]. Compared to the other two methods, wafer-to-wafer stacking has the main advantages of uniform integration and maximum

How to cite:
Q. Yang et al., "Polypropylen Carbonate Based Temporary Bonding/ Debonding Triggered by Microwave", Inf. Midem-J. Microelectron. Electron. Compon. Mater., Vol. 53, No. 3(2023), pp. 225–231

throughput (as long as the device wafer yield is high) [9], thereby reducing costs. However, thicker wafers are difficult to meet the heat dissipation and packaging requirements of high-end chips, and often require the thinning of the wafer to the desired thickness. When the wafer thickness is reduced to below 200μm, ultra-thin wafers become brittle and prone to warping [10]. Therefore, the semiconductor industry has proposed various temporary bonding/debonding technologies to temporarily bond the device wafer to a thicker rigid carrier substrate using an appropriate adhesive [11].

The methods of debonding can be divided into thermal slide-off debonding, chemical debonding, mechanical debonding, and laser debonding [12,13,14]. The drawback of thermal slide-off debonding is the requirement of high temperature, which may not be suitable for some ultra-thin wafers that cannot withstand high-temperature treatment. Additionally, the process of an ultra-thin wafer sliding off the carrier wafer may lead to damage. Chemical debonding involves immersing the bonded substrate into a chemical solution to release the bonding adhesive. However, uncontrolled floating of the device substrate in the solvent bath during and after debonding may cause device failure [15]. Mechanical debonding is a relatively aggressive method of separating ultra-thin wafers from carrier wafers at room temperature using special tools, but it may lead to damage due to the thin and brittle nature of ultra-thin wafers. Laser ablation of the sacrificial polymer layer is another method for temporary chip handling. However, the moment of laser corrosion can generate localized high temperatures, which may damage the entire bonded wafer. This method has also been used for controlled transfer of molds between two wafers, such as using polyimide or PET as an adhesive for manufacturing low-cost AFM devices [16]. Debonding is expensive, requiring specialized decryption equipment and taking a long time. PPC (polypropylene carbonate) is a polymer of propylene oxide and carbon dioxide. This polymer has biodegradable properties and can be used for disposable applications. In the field of bonding technology, PPC is readily available, and its excellent adhesive strength allows reconfigured wafers to withstand mechanical grinding. Additionally, its thermal decomposition properties enable easy separation of ultra-thin chips from the carrier wafer by heating the bonded pair to a relatively low temperature. The bonding strength of PPC is dependent on the concentration of the bonding solution, and the bonding effect of PPC varies at different bonding temperatures [17].

In order to overcome the above-mentioned shortcomings, extensive research was conducted in this study on a temporary bonding/debonding scheme based on PPC. A controlled experiment was designed, and ultimately a bonding structure utilizing a microwave heating environment, with PPC as the primary adhesive, a moderate amount of PAG, and graphite powder, was developed. The highest average shear strength achieved was 5.1 MPa. During the debonding process, microwave heating of the graphite powder was utilized, which then transferred heat to the bonding layer, causing the acid generator within the bonding layer to decompose at a lower temperature, leading to the decomposition of the entire bonding layer and achieving rapid and convenient debonding. This temporary bonding/debonding scheme is cost-effective and functionally efficient.

2 Design and experiment

2.1 Bonding/debonding principle

The paper proposes a fast, efficient, and convenient temporary bonding solution using microwave heating of the bonding layer. A microwave oven is a common household appliance used for heating food, operating on the principle of generating microwaves inside the cavity to create a uniform microwave electric field. Although microwaves do not produce heat on their own, when concentrated and directed onto an object capable of absorbing microwaves, the polar molecules within the object undergo intense movement, similar to friction, resulting in the heating of the object and the generation of heat. Graphite powder is capable of absorbing microwaves and generating heat; for instance, when applied to paper, it can even burn a hole through it. In terms of thermodynamics, amorphization is an unfavorable process at equilibrium. When certain materials (e.g., silicon wafers) in the exposed area are directly heated by microwaves, crystallization occurs, while the metal-coated area, which shields radiation and undergoes indirect heating, does not experience crystallization. These results indicate that certain areas of the sample can be shielded with a metal coating to prevent crystallization, while exposed areas can undergo microwave-induced crystallization [18]. The glass substrate used in this experiment does not undergo crystallization during the microwave annealing process .

The main concept of this approach involves using PPC as the primary adhesive and adding a controlled amount of PAG and graphite powder to achieve temporary bonding of two glass pieces. When debonding is required, the bonded piece is placed in a microwave oven. The microwave heats the graphite powder, which then transfers the heat to the bonding layer, causing the acid generator within the bonding layer to decom-

pose. This triggers the breakdown of the entire bonding layer, ultimately achieving rapid and convenient debonding, as shown in Fig. 1.

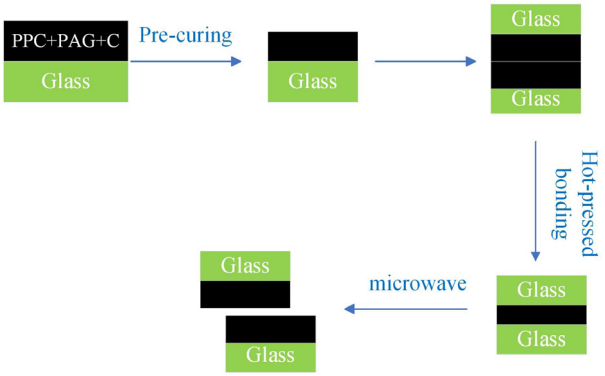

Figure 1: The principle of bonding/ microwave debonding process based on PPC+PAG+C.

2.1 Design of Experiments

Investigation of baking parameters

Procedure: Prepare a 20% mass fraction PPC solution and coat the PPC solution onto a glass wafer. Place glass slides in oven set at different temperatures for solvent evaporation, and then use a hot press to bond the wafers in the air environment. The baking parameters are as follows: temperatures of 70°C, 100°C, and 130°C and baking times of 30 minutes, 30 minutes, and 5 minutes, respectively. Finally, obtain the bonded glass wafer and conduct a residual stress test after it has cooled.

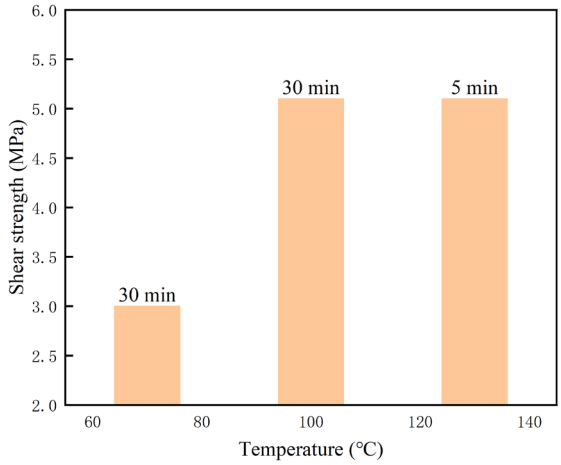

Figure 2: Maximum shear strength of the bonding sheet at different baking temperatures for 20wt%PPC.

Fig. 2 shows that baking at 70°C for 30 minutes resulted in a shear strength of only 3.1 MPa, which falls far short of the desired outcome. This may be due to the temperature being insufficient, leading to slow solvent removal. As a result, after cooling, some solvents may not have been completely removed, causing a loose internal structure in the bonding layer. Increasing the temperature to 100°C resulted in a shear strength of 5.1 MPa, which is more in line with expectations. Further rise of the temperature to 130°C allowed achieving the same effect in just 5 minutes, compared to the 30 minutes required at 100°C what significantly reduced the bonding time and enhance the efficiency of the bonding process.

Investigation of PPC concentration

Bonded glass slides using adhesive with PPC mass fractions of 15%, 20%, and 25% by using baking parameters at 130°C for 5 minutes were prepared. The bonding strength using a shear stress tester (Flat-push tester), for different PPC concentrations, was measured and the result is shown in Fig. 3.

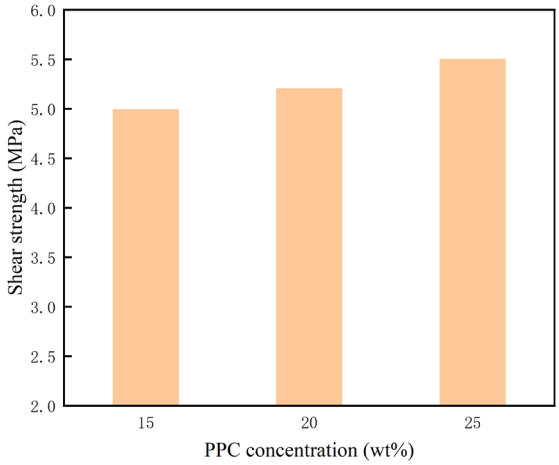

Figure 3: Shear strength of bonding sheets for different PPC concentrations.

The bonding strength is highest for the 20% mass fraction of PPC adhesive, with a shear strength of 5.5 MPa. For the 25% mass fraction, the shear strength is 5.2 MPa and the lowest is for the 15% mass fraction of PPC, at only 4.99 MPa. The photo acid generator (PAG) used in the experiment is 4-isopropyl-4'-methyl-diphenyliodonium tetra(pentafluorophenyl)borate, developed by TCI Corporation. It is capable of generating a large amount of acidic substance starting at 200 °C without UV light exposure. With UV light exposure, it can slowly start acid generation at 100°C. Additionally, the addition of copper powder as a catalyst in the PAG can lower the temperature at which acid generation begins [19,20]. The substrate used is glass and is chosen because, unlike silicon, it does not hinder the absorption of microwaves.

In order to verify if the addition of graphite powder in the (PPC-PAG) adhesive allows debonding with microwaves at lower temperatures and to study the phenomena during debonding the following preliminary experiment was conducted, as shown schematically in Fig. 4.

Experimental Scheme

The pre-mixed PPC-PAG solution was applied to two glass pieces for pre-curing. Pre-curing refers to the curing of the bonding agent before baking. The purpose of this step is to allow the bonding agent to lose some of its solvents, forming a shape with a raised edge and a concave center. Dry graphite powder(15 mg) was then added to a 100mm^2 glass piece and flattened to ensure good contact with the bonding layer while maintaining good compaction. The bonding was then carried out using a hot press according to the parameters shown in Table 1. During this period, the bonded piece with added graphite was tested while still in the bonded state. After cooling down from bonding, the glass pieces were placed in a Panasonic DS2000 microwave oven with 1000 W of power at a frequency of 2.45 GHz along with a cup of water to prevent accidents. The pieces were exposed to microwaves for a certain period of time to achieve debonding The experimental results will be discussed in Section 3.

Table 1: Adhesives and bonding parameters

Parameter	Value	
Bond serial number	1	2
PPC quantity vol. (%)	20	20
PAG quantity vol. (%)	5	5
Graphite amount (mg)	15	0
Pre-curing temperature (°C)	25	25
Pre-curing time (min)	1	1
Curing temperature (°C)	130	130
Curing time (min)	5	5
Pressure (MPa)	0.2	0.2

In comparison to the preliminary experiment, three temporary bonding options were prepared to test the effectiveness of microwaves in heating the bonding layer for debonding.

The determination of graphite parameters for the three options is shown in Table 2, while the bonding agent uses 20wt% PPC and 5wt% PAG. The three bonding options, depicted as Options A, B, and C are shown in Fig. 4. Option A involves directly mixing graphite into the adhesive, thoroughly stirring it, applying it to the glass slide, and then bonding it using microwave heating. Option B utilizes water-soluble graphite with better microwave absorption properties in the pencil tip, allowing it to achieve higher temperatures when subjected to the same microwave exposure, furthermore, in B paper is coated with graphite on both sides and placed between the bonding layers to ensure evenly distribution of graphite powder on the white paper. In Option C, after pre-curing the glass slide, graphite powder is added and compacted in the central part of the glass slide, followed by solidification bonding.

Table 2: Selection of graphite parameters

Option	Graphite quantity	Graphite composition	Paper area
A	15 mg	Graphite powder	\
B	Covering a piece of paper	Water-soluble pencil	1cm^2
C	15 mg	Graphite powder	\

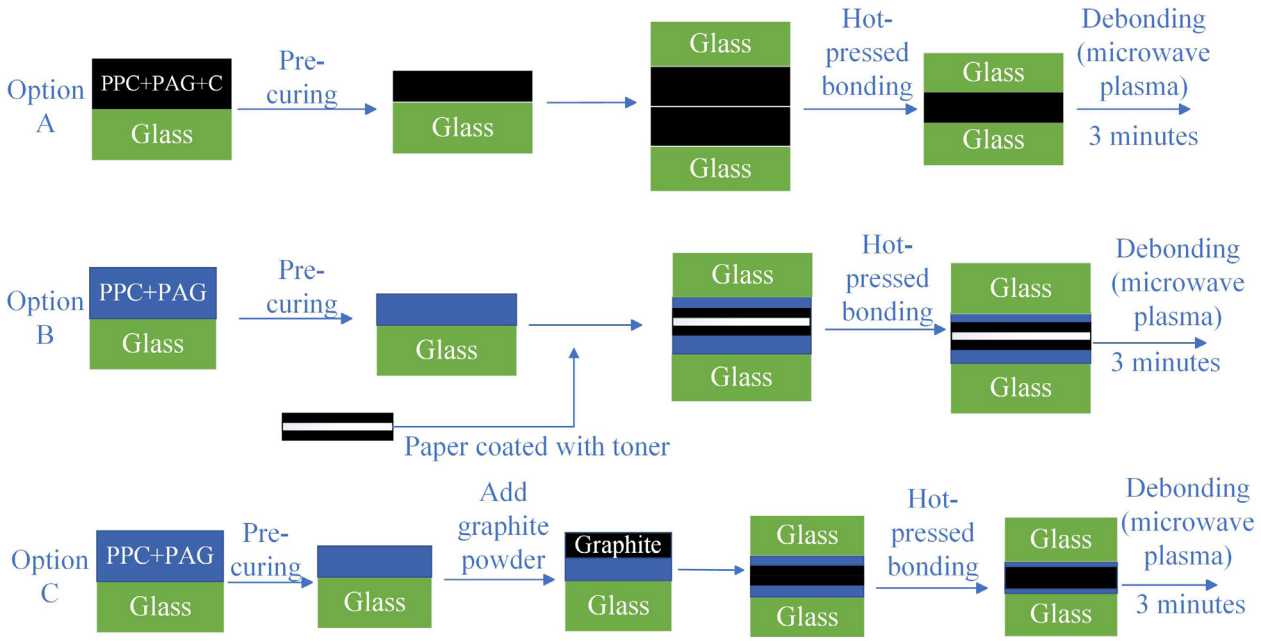

Figure 4: Three temporary bonding options marked as Option A, B, C. Debonding is the same for all bonded options, i.e. microwave treatment took 3 minutes.

3 Results and discussion

Our experimental results show that after adding graphite to the original bonding option (PPC+PGA) the shear strength of the bond can still be maintained at the same level. Fig. 5 shows the appearance of the two glass sheets with and without the addition of graphite powder in the bonding layer after heating at 180°C for 5 minutes. The bonding layer produced a reddish-brown substance due to acid decomposition and reaction with the PPC adhesive, forming a liquid with flow-like properties and emitting a certain amount of irritating gas. Because the graphite powder has a certain particle size, some cavities are formed in the middle, containing a mixture of gases produced by the decomposition of the adhesive and air. The presence of air inside the cavities leaked in during the decomposition process when the gas slightly lifted the glass sheet. After cooling, the remaining material was measured for bonding strength as shown in Fig. 6. It can be observed that the bonding strength of the remaining material bonding layers has significantly decreased. The maximum shear strength of PPC+PAG is 2.98 MPa, while PPC+PAG+C is 3.99 Mpa. The bonding strength of the adhesive with added graphite is stronger than that without graphite, possibly because the addition of graphite increases friction, resulting in a greater force required to push open when measuring the shear stress. Fig. 7 shows the separated glass sheets.

(a)

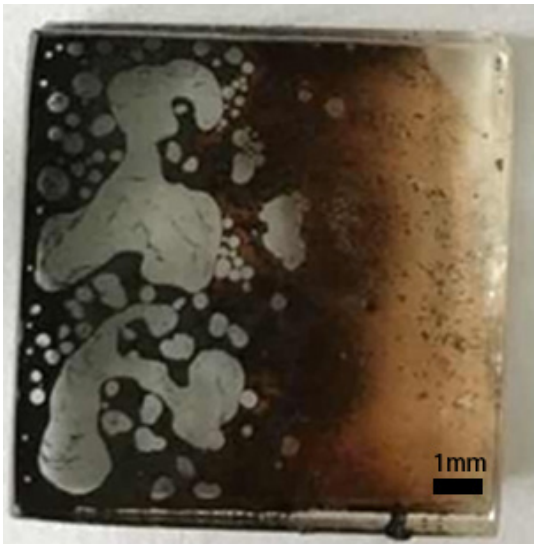

(b)

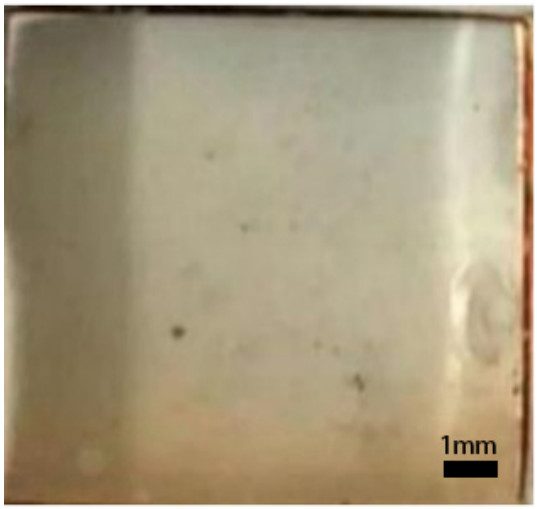

Figure 5: Heating the bonding samples at 180°C for 5 min: (a) with and (b) without added powder graphite.

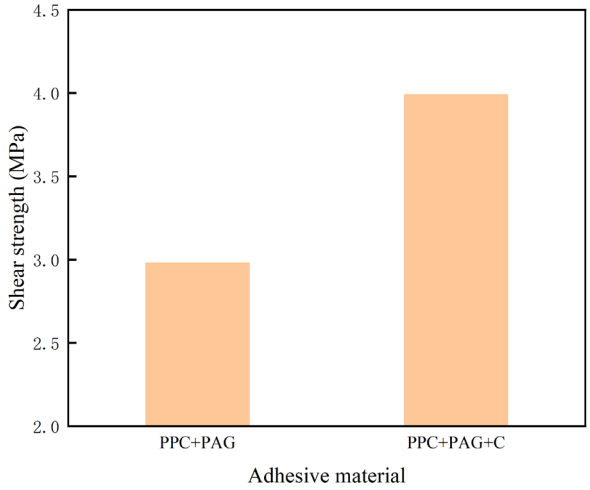

Figure 6: Shear strength of bonded samples for process without and with added powder graphite.

In Option A, the bonded sheets showed no significant temperature change after microwave treatment because the heat generated during the graphite bonding was diluted by the adhesive, preventing it from concentrating. In Option B, the bonded sheets also showed no significant temperature change after microwave treatment because when the graphite was applied to the paper, most of the contact area was with the paper rather than the adhesive, so any heat generated was unlikely to propagate to the adhesive or the glass surface. In Option C, the bonded sheets showed a significant overall temperature increase for at least 100°C after microwave treatment, along with a noticeable pungent odor from the decomposition of the acid and its reaction with the PPC. Some of the adhesive on the glass has disappeared, and the remaining adhesive is mixed with graphite powder. Through comparison with the control group, the bonded sheets just removed from the microwave could be pushed open manually with a tool, and the surface of the adhesive exhibited a filamentous appearance, indicating that the required temperature for bonding had been achieved. In summary, options A and B were unable to generate sufficient heat for debonding with microwave plasma treatment, while the process C successfully demonstrate use of microwaves for rapid and convenient debonding.

(a)

(b)

Figure 7: Stripped bonding piece after debonding (a) with and (b) without added powder graphite.

After comparing the three experimental bonding/debonding option, it can be concluded that process option C is the most effective. In this process, the bonded sheets showed the formation of a yellow-brown substance on the surface after microwave treatment what require less force to debond. The adhesive appeared in a liquid state and the glass sheet remains undamaged. This process scheme of temporary bonding/debonding it met all the expectations of the experiment such as low cost and high efficiency.

4 Conclusions

In this work the temporary bonding solutions using a photogenerated acid generator (PAG) and graphite powder © as a load for polypropylene carbonate (PPC), with the bonding layer heated by microwaves to achieve a fast, efficient, and convenient bonding/debonding process were investigated. For the (PPC+PAG+C) bonding structure, the highest average shear strength reached 5.1 Mpa. For the debonding process, microwaves were used to heat the graphite powder, which then transferred heat to the bonding layer, causing the acid generator inside the bonding layer to decompose at room temperature, leading to the collapse of the entire bonding layer and thus it is achieved rapid and convenient debonding.

Among the three different process options introduction of powder graphene in the bonding/debonding scheme, only the process option C resulted in efficient debonding with microwaves at room temperature.

5 Acknowledgments

This work was supported by the Open Research Fund of China National Key Laboratory of Materials for Integrated Circuits (NKLJC-K2023-12), Hubei Key Laboratory of Electronic Manufacturing and Packaging Integration (No. EMPI2023012) and National Natural Science Foundation of China (62074132).

6 Conflict of interest

The authors declare that there are no conflict of interests.

7 References

1. Boukortt, N., Patanè, S. & Crupi, G. 3D Investigation of 8-nm Tapered n-FinFET Model. Silicon 12, 1585–1591 (2020), https://doi.org/10.1007/s12633-019-00253-y.
2. Matthias, T., Wimplinger, M., Pargfrieder, S. et al. 3D Process Integration – Wafer-to-Wafer and Chip-to-Wafer Bonding. MRS Online Proceedings

Library 970, 408 (2006), https://doi.org/10.1557/PROC-0970-Y04-08.
3. M. Koyanagi, T. Fukushima, and T. Tanaka, "High-Density Through Silicon Vias for 3-D LSIs," Proc. IEEE, vol. 97, pp.49-59, Jan. 2009, https://doi.org/10.1109/JPROC.2008.2007463.
4. D.J. Bartelink, "Integrated Systems," IEEE Trans. Electron Dev., vol. 43, pp1678-1687, 1996, https://doi.org/ 10.1109/16.536814.
5. A. Klumpp, R. Merkel, R. Wieland, and P. Ramm, "Chip to Wafer Stacking Technology for 3D System Integration," Proceedings of 53rd Electronic Components and Technology Conference, p.1080, 2003, https://doi.org/10.1109/ECTC.2003.1216424.
6. T. Fukushima, H. Hashiguchi, J. bea, Y. Ohara, M. Murugesan, K. Lee, T. Tanaka, M. Koyanagi, "New Chip-to-Wafer 3D Integration Technology Using Hybrid Self-Assembly and Electrostatic Temporary Bonding," 2012 IEEE International Electron Devices Meeting, p. 789, 2012, https://doi.org/ 10.1109/IEDM.2012.6479157.
7. P. Lindner, V. Dragoi, T. Glinsner, C. Schaefer, and R. Islam, "3D Interconnect through Aligned Wafer Level Bonding," Proceedings of 52nd Electronic Components and Technology Conference, p.1439, 2002, https://doi.org/10.1109/ECTC.2002.1008295.
8. T. Fukushima, J. Bea, H. Kino, C. Nagai, M. Murugesan, H. Hashiguchi, K.W. Lee, T. Tanaka, and M. Koyanagi, "Reconfigured-Wafer-to-Wafer 3-D Integration Using Parallel Self-Assembly of Chips With Cu-SnAg Microbumps and a Nonconductive Film," IEEE Trans. Electron Dev., vol. 61, pp. 533-539, 2014, https://doi.org/10.1109/TED.2013.2294831.
9. M. Murugesan et al., "Back-via 3D integration technologies by temporary bonding with thermoplastic adhesives and visible-laser debonding," 2016 International Conference on Electronics Packaging (ICEP), Hokkaido, Japan, 2016, pp. 265-269, https://doi.org/10.1109/ICEP.2016.7486825.
10. Landesberger, C.; Klink, G.; Schwinn, G.; Aschenbrenner, R. New dicing and thinning concept improves mechanical reliability of ultra thin silicon. In Proceedings of the Proceedings International Symposium on Advanced Packaging Materials Processes,Properties and Interfaces (IEEE Cat. No.01TH8562), Braselton, GA, USA, 11–14 March 2001; pp. 92–97, https://doi.org/ 10.1109/ISAOM.2001.916555.
11. Puligadda, R.; Pilialamarri, S.; Hong, W.; Brubaker, C.; Wimplinger, M.; Pargfrieder, S. High-performance temporary adhesives for wafer bonding applications. Mater. Res. Soc. Symp. Proc. 2006, 970, 239–256, https://doi.org/10.1557/PROC-0970-Y04-09.
12. X. Shuai, R. Sun, G. Zhang and L. Deng, "A novel temporary adhesive for thin wafer handling," 2014 15th International Conference on Electronic Packaging Technology, Chengdu, China, 2014, pp. 256-261, https://doi.org/10.1109/ICEPT.2014.6922649.
13. Mo, Z.; Wang, F.; Li, J.; Liu, Q.; Zhang, G.; Li, W.; Yang, C.; Sun, R. Temporary Bonding and Debonding in Advanced Packaging: Recent Progress and Applications. Electronics 2023, 12, 1666, https://doi.org/ 10.3390/electronics12071666.
14. Zussman, Melvin P. et al. "Using Permanent and Temporary Polyimide Adhesives in 3D-TSV Processing To Avoid Thin Wafer Handling." Journal of microelectronics and electronic packaging 7 (2010): 214-219, https://doi.org/10.4071/2010DPC-TP16.
15. Tan, C. S., Chen, K.-N., & Koester, S. J. (2012). 3D integration for VLSI systems. Singapore: Pan Stanford Pub, https://doi.org/10.4032/9789814303828.
16. H. K. Gatty, F. Niklaus, G. Stemme and N. Roxhed, "Temporary wafer bonding and debonding by an electrochemically active polymer adhesive for 3D integration," 2013 IEEE 26th International Conference on Micro Electro Mechanical Systems (MEMS), Taipei, Taiwan, 2013, pp. 381-384, https://doi.org/10.1109/MEMSYS.2013.6474258.
17. X. Xue, S. Yang, D. Wu, L. Pan and Z. Wang, "Fabrication of ultra-thin silicon chips using thermally decomposable temporary bonding adhesive," 2016 IEEE SENSORS, Orlando, FL, USA, 2016, pp. 1-3, https://doi.org/10.1109/ICSENS.2016.7808438.
18. Amin Nozariasbmarz, Kelvin Dsouza, Daryoosh Vashaee; Field induced decrystallization of silicon: Evidence of a microwave non-thermal effect. Appl. Phys. Lett. 26 February 2018; 112 (9): 093103. https://doi.org/10.1063/1.5020192
19. Zhu, Z., Yu, M., Liu, L., and Jin, Y. (October 20, 2015). "Temporary Bonding/Debonding of Silicon Substrates Based on Propylene Carbonate." ASME. J. Electron. Packag. December 2015; 137(4): 044501, https://doi.org/10.1115/1.4031750.
20. Zhu Z , Xu Z . PPC-based bilayer temporary bonding and debonding[J]. Microelectronic Engineering, 2017, 180:5-7, https://doi.org/10.1016/j.mee.2017.05.029.

Copyright © 2023 by the Authors. This is an open access article distributed under the Creative Commons Attribution (CC BY) License (https://creativecommons.org/licenses/by/4.0/), which permits unrestricted use, distribution, and reproduction in any medium, provided the original work is properly cited.

Arrived: 30. 12.2 023
Accepted: 07. 02. 2024

Original scientific paper
https://doi.org/10.33180/InfMIDEM2023.403

Informacije MIDEM
Journal of Microelectronics, Electronic Components and Materials
Vol. 53, No. 4(2023), 233 – 238

Linear Thermal Expansion of $0.5Ba(Zr_{0.2}Ti_{0.8})O_3$-$0.5(Ba_{0.7}Ca_{0.3})TiO_3$ Bulk Ceramic

Sabi William Konsago[1,2], Andrej Debevec[1], Jena Cilenšek[1], Brigita Kmet[1,2], Barbara Malič[1,2]

[1]Electronic Ceramics Department, Jožef Stefan Institute, Ljubljana, Slovenia
[1]Jožef Stefan International Postgraduate School, Ljubljana, Slovenia

Abstract: We report the linear thermal expansion coefficient of lead-free ferroelectric ceramic barium zirconate titanate - barium calcium titanate $0.5Ba(Zr_{0.2}Ti_{0.8})O_3$-$0.5(Ba_{0.7}Ca_{0.3})TiO_3$ (BZT-BCT). The material was prepared by solid-state synthesis and consolidated by sintering at 1450°C. BZT-BCT crystallizes in the perovskite phase. The microstructure of the ceramic with about 95 % relative density consists of about 10 μm-sized grains. The contact dilatometry of the ceramic specimen reveals the change of slope of the linear thermal expansion curve at 84°C. This is in good agreement with the peak of the dielectric permittivity versus temperature at about 85°C indicating the transition from the low-temperature polar ferroelectric phase to a high-temperature nonpolar phase or Curie temperature. The thermal expansion coefficients of the polar tetragonal and nonpolar cubic phases of BZT-BCT are 7.69×10^{-6} K^{-1} (40°C – 80°C) and 12.39×10^{-6} K^{-1} (100°C – 600°C), respectively. The thermal expansion data are among the material data needed in the design of thin- and thick-film structures for energy-harvesting and energy-storage applications.

Keywords: $0.5Ba(Zr_{0.2}Ti_{0.8})O_3$-$0.5(Ba_{0.7}Ca_{0.3})TiO_3$ (BZT-BCT), lead-free, ferroelectric ceramic, linear thermal expansion

Linearni temperaturni raztezek volumenske keramike $0.5Ba(Zr_{0.2}Ti_{0.8})O_3$-$0.5(Ba_{0.7}Ca_{0.3})TiO_3$

Izvleček: V delu poročamo o linearnem temperaturnem raztezku volumenske keramike barijevega cirkonata titanata - barijevega kalcijevega titanata $0.5Ba(Zr_{0.2}Ti_{0.8})O_3$-$0.5(Ba_{0.7}Ca_{0.3})TiO_3$ (BZT-BCT). Material smo pripravili s sintezo v trdnem stanju in sintranjem pri 1450°C. BZT-BCT kristalizira v perovskitni fazi. Mikrostrukturo keramike s ≈95% relativno gostoto sestavljajo zrna velikosti okrog 10 μm. Linearni temperaturni raztezek keramike smo izmerili s kontaktno dilatometrijo od sobne temperature do 600°C. Pri temperaturi 84°C opazimo spremembo naklona krivulje raztezka. Ta podatek se ujema s temperaturo maksimuma dielektričnosti v odvisnosti od temperature, ki označuje prehod nizkotemperaturne polarne feroelektrične faze v visokotemperaturno nepolarno fazo oziroma Curiejevo temperaturo. Vrednosti linearnega temperaturnega raztezka polarne in nepolarne faze BZT-BCT sta 7.69×10^{-6} K^{-1} (40°C – 80°C) in 12.39×10^{-6} K^{-1} (100°C – 600°C). Podatke o temperaturnem raztezku keramike potrebujemo pri načrtovanju tanko- in debeloplastnih struktur, namenjenih zbiranju in shranjevanju energije.

Ključne besede: $0.5Ba(Zr_{0.2}Ti_{0.8})O_3$-$0.5(Ba_{0.7}Ca_{0.3})TiO_3$ (BZT-BCT), brez svinca, feroelektrična keramika, linearni temperaturni raztezek

** Corresponding Author's e-mail: barbara.malic@ijs.si*

1 Introduction

The discovery of the high piezoelectric properties of the barium zirconate titanate - barium calcium titanate solid solution $0.5Ba(Zr_{0.2}Ti_{0.8})O_3$-$0.5(Ba_{0.7}Ca_{0.3})TiO_3$ (BZT-BCT) bulk ceramic has revealed its great potential for many piezoelectric applications including actuators, transducers, and energy harvesting devices [1] - [3]. As an example, an intravascular ultrasound transducer made of BZT-BCT has been prototyped [4]. It is also being studied as a promising biocompatible material for bone regeneration [5], [6]. BZT-BCT has gained the attention of the ferroelectric/piezoelectric communities as one of the most promising environment-friendly alternatives to commercially widely spread lead-based piezoelectric ceramic materials such as $Pb(Zr,Ti)O_3$ (PZT) due to the Restriction of Hazardous Substances

How to cite:
S. W. Konsago et al., "Linear Thermal Expansion of $0.5Ba(Zr_{0.2}Ti_{0.8})O_3$-$0.5(Ba_{0.7}Ca_{0.3})TiO_3$ Bulk Ceramic", Inf. Midem-J. Microelectron. Electron. Compon. Mater., Vol. 53, No. 3(2023), pp. 233–238

(RoHS) regulations [7] - [9]. Recently it has been reported that it possesses promising energy storage properties [10], [11].

BZT-BCT exhibits a Curie temperature of about 85-90 °C. In the proximity of room temperature, the coexistence of rhombohedral, orthorhombic, and tetragonal phases of solid solutions of $Ba(Zr_{0.2}Ti_{0.8})O_3$ and $(Ba_{0.7}Ca_{0.3})TiO_3$ with the molar ratios close to unity contributes to enhanced piezoelectric properties [12], [13]. It was shown that the grain size strongly influences the piezoelectric properties and the phase transitional behaviour of BZT-BCT bulk ceramic; the enhanced piezoelectric response was characteristic for grain sizes exceeding 10 μm [14].

In numerous miniature devices, such as microelectromechanical systems (MEMS) or energy harvesters, the space constraints favour the use of piezoelectric ceramic elements in the form of thin or thick films [15], [16]. One of the key parameters for designing such devices includes the thermal expansion coefficients of the constituent materials. In case of a large difference in thermal expansion coefficients of the film and the substrate, the induced stresses may contribute to lowering the piezoelectric response [17] - [19]. Clamping the screen-printed thick film by the substrate results in poor densification during sintering [20]. Tensile stresses in the film that arise due to the thermal expansion coefficient mismatch may lead to the evolution of cracks [19]. Various effects of stresses generated by the thermal expansion mismatch also affect other functional properties, such as breakdown strength [21], [22], which is important in energy storage applications.

There are some publications on the thermal expansion coefficient of Ca- and Zr-modified barium titanate ceramics [23] - [26] but to our knowledge, there is no reported study on the linear thermal expansion coefficient of BZT-BCT ceramic. Such data would contribute to efficiently designing the processing of dense and crack-free BZT-BCT thick films where the powder slurry is screen-printed on a platinized alumina substrate. Such films could find applications in energy harvesting.

Our study aims to prepare perovskite BZT-BCT ceramic with a high relative density, uniform microstructure, and adequate low- and high-field dielectric properties. The linear thermal expansion coefficient from room temperature to 600 °C is measured.

2 Materials and methods

BZT-BCT powder was prepared using alkaline earth carbonates ($BaCO_3$, 99.8% and $CaCO_3$, 99,95% both from Alfa Aesar, Karlsruhe, Germany) and transition metal oxides (TiO_2, 99.8% also from Alfa Aesar, Karlsruhe, Germany and ZrO_2, 99.8% from Tosoh, Japan). The metal content was checked gravimetrically. The 25 g batches of stoichiometric fractions of the reagents were homogenized using isopropanol in a planetary mill (PM 400, Retsch) with yttria-stabilized zirconia milling bodies (3 mm, Tosoh, Japan) for 2 h at 200 rpm. The median particle size of the milled powder was 0.45 μm as determined by laser granulometry (Microtrac S3500 Particle Size Analyzer) using isopropanol as a dispersion liquid. The calcination of the loosely pressed reagent mixture (P = 50 MPa) took place at 1300 °C for 4 hours in the air with heating and cooling rates of 5 K/min. The powder was again milled for 2h at 200 rpm in a planetary mill, dried at 120 °C and sieved. The powder was shaped into pellets (diameter: 8 mm) or bars (40 mm x ≈7 mm x ≈5 mm) by uniaxial (P = 50 MPa) and isostatic pressing (P = 300 MPa). The powder compacts were sintered at 1450 °C for 4 hours in the air with heating and cooling rates of 5 K/min.

The phase composition of the calcined powders and crushed sintered specimens was analyzed by X-ray diffraction (XRD, X'Pert PRO MPD, PANanalytical, CuKa1 radiation, time/step: 100 s, interval between data points: 0.0016°). The density of the sintered samples was determined pycnometrically (Micromeritics, AccuPyc III 1340 Pycnometer).

The ceramic samples were ground and polished using standard ceramographic techniques. Thermal etching of the polished sections at 1350 °C for a few minutes revealed the grain boundaries. A field-emission scanning electron microscope (FE-SEM JEOL JSM-7600) with an energy-dispersive X-ray spectrometer (EDXS, INCA Oxford 350 EDS SDD) was used for the analysis of the microstructure. The grain size was determined using the Image Tool software.

For low- and high-field dielectric measurements, the disks were cut to the thickness of 0.5 mm and polished. An annealing step to 600 °C for 1 h followed by a slow cooling (1 K/min) was used to release the stresses of mechanical operations. The Au electrodes with a diameter of 3 mm were RF-magnetron sputtered on the faces of the disks (5 Pascal). The dielectric permittivity (ε) and losses ($\tan\delta$) were measured between +150 °C and -40°C with a cooling rate of 1 K/min (Agilent E4980A Precision LCR meter, 1V). The polarization-electric field hysteresis loops were measured at room temperature with a sine voltage at the frequency of 50 Hz (Aixacct TF analyzer 2000).

For the measurement of the thermal expansion, the ceramic bars were cut to the dimensions of 25 mm x 5 mm x 4 mm. The faces of the bars were plan-parallel

polished. Thermal stresses were released as described above. The dimensional changes of the specimen upon heating and cooling were measured with a contact dilatometer with a corundum measuring system (Netzsch DIL 402 PC) between room temperature and 600 °C with the heating and cooling rates of 5 K/min in air.

3 Results and discussion

Figure 1 contains the XRD patterns of BZT-BCT powder after the calcination at 1300 °C (a) and the ceramic sintered at 1450 °C (b). The XRD patterns of both samples reveal a perovskite phase without any noticeable secondary phases. The unit cell distortion could not be determined using a standard X-ray diffractometer, synchrotron radiation would be needed to obtain a deeper insight into the phase composition of the material, c.f. [13], [27] - [29]. According to the phase diagram [13], the coexistence of the orthorhombic phase cannot be excluded at room temperature besides rhombohedral and tetragonal phases in the morphotropic phase boundary region.

The relative density of BZT-BCT ceramic is 95.4 %. The microstructure shown in Figure 2 a) is uniform, with a unimodal grain size distribution and a mean grain size of 9.66 ± 4.84 μm (Figure 2 b)). EDXS analysis confirmed a uniform distribution of elements within and between individual grains (EDXS spectra are not shown). Trace amounts of a secondary phase were observed at some grain junctions (see the inset of Figure 2 a)) but due to their small size, their chemical composition could not be reliably determined on the level of FE-SEM.

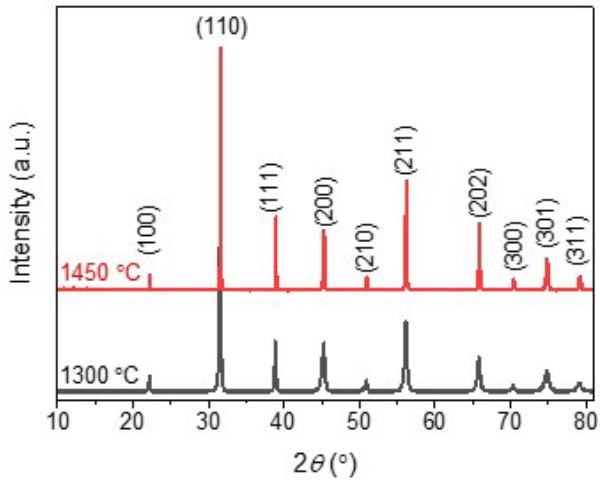

Figure 1: XRD patterns of BZT-BCT powder calcined at 1300 °C and ceramic sintered at 1450 °C. The peaks are indexed according to the $BaTiO_3$ cubic phase (PDF 01-074-4539).

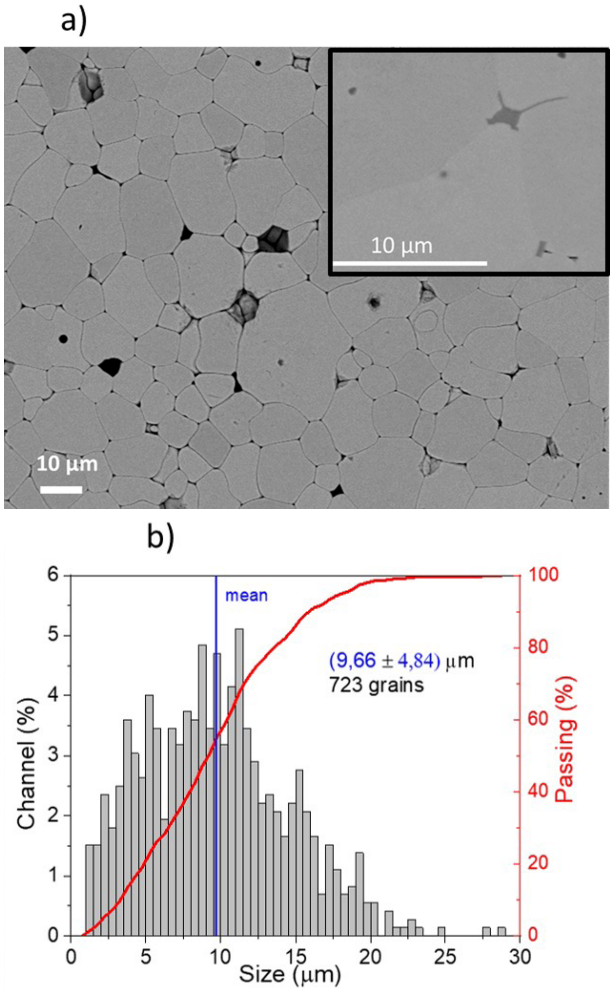

Figure 2: a) SEM micrograph of the microstructure of BZT-BCT ceramic and b) grain size distribution. Inset in panel a) reveals an intergranular phase located at a grain junction.

Figure 3 shows the temperature dependence of the dielectric permittivity and losses as a function of temperature in the frequency range from 100 Hz to 100 kHz. Dielectric permittivity and losses at room temperature and 1 kHz are 3165 and 0.029 in agreement with reported values for ceramics with similar grain sizes [14]. There is no significant change in the dielectric permittivity in the frequency range from 100 Hz to 100 kHz in the measured temperature range. The change of slope at about 40 °C is attributed to the rhombohedral–tetragonal phase transition, and the dielectric permittivity peak at about 85 °C to transition to the cubic phase or Curie temperature. The grain size influences both phase transition temperatures; for the ceramic with about 10 μm-sized grains, the respective values were 87 °C and 35 °C [14]. Broadening of the permittivity peak, characteristic of polycrystalline ferroelectrics, is related to the micron size of the crystallites and the presence of two cations on each cation sublattice

site. We do not observe any noticeable frequency peak shifting in the measured frequency range supporting the ferroelectric nature of the BZT-BCT ceramic. It has been shown that processing conditions and grain size strongly influence the ferroelectric or relaxor nature of BZT-BCT [14], [27].

Figure 4 shows the room temperature polarization–electric field (*P–E*) hysteresis loops measured at 50 Hz. The sample survived the maximum applied field of 70 kV/cm, indicating its good dielectric breakdown resistance. The remnant polarization P_r and coercive field E_c are about 13 μC/cm^2 and 5.9 kV/cm, respectively, indicating a good ferroelectric response of BZT-BCT. Hao et al obtained similar P_r and E_c values for the ceramic with 10 μm-sized grains [14].

Figure 5 shows the dilatometric curves of BZT-BCT ceramic, revealing linear thermal expansion or contraction upon heating or cooling. There is not much difference between the heating and cooling curves. Two main slopes are discerned in both cases with the inflexion point at 84.0 °C. The thermal hysteresis between the heating and cooling runs is quite small. We note that the inflexion temperature corresponds well to the dielectric permittivity peak temperature, cf. Figure 3. The thermal expansion coefficient (TEC = $(\Delta L/L_0)/\Delta T$), determined from the cooling curve in the temperature range from 40 °C to 80 °C, is 7.69×10^{-6} K^{-1}. In this temperature range the tetragonal phase prevails [13], but the coexistence of a rhombohedral phase cannot be excluded judging from the evident change of slope at about 40 °C in the dielectric permittivity curve (cf. Figure 3). As the temperature increases, the TEC progressively increases as well. From 100 °C to the final temperature of 600 °C, in the temperature range of the cubic phase, the TEC is 12.39×10^{-6} K^{-1}.

As explained earlier we could not find the thermal expansion data for BZT-BCT. The TEC of the base formulation of BZT-BCT solid solution, the prototype ferroelectric $BaTiO_3$, is 6.5×10^{-6} K^{-1} in the tetragonal phase and 9.8×10^{-6} K^{-1} in the cubic phase (125 °C – 200 °C) measured by contact dilatometry [30]. It is noted that the change in the slope of the thermal expansion of $BaTiO_3$ at the phase transition temperature is sharp and accompanied by a noticeable shrinkage which is a fingerprint of a first-order phase transition and is not the case with BZT-BCT. Here, we observe only the change in the slope of the thermal expansion. Tian et al. studied $(Ba,Ca)TiO_3$-$Ba(Zr,Ti)O_3$ with slightly different molar ratios of cations compared to BZT-BCT formulation, and they incorporated various rare-earth dopants. They measured a TEC of about 5×10^{-6} K^{-1} at lower temperatures and a TEC of about 11×10^{-6} K^{-1} at higher temperatures, the final temperature being 400 °C. The exact value of TEC and the TEC-inflexion point's temperature depended on the studied materials' chemical composition[31], [32]. Our results are in good agreement with these latter dilatometric studies of the $(Ba,Ca)TiO_3$-$Ba(Zr,Ti)O_3$ solid solutions.

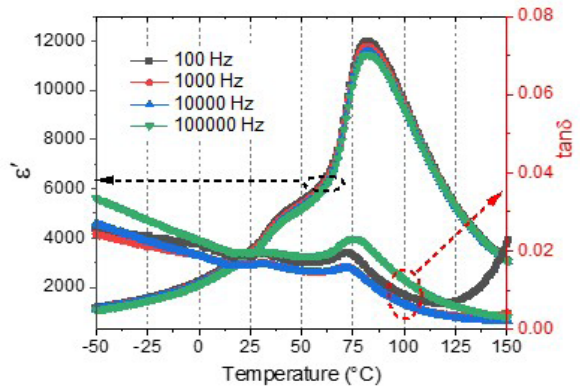

Figure 3: The dielectric permittivity and losses as a function of the temperature of BZT-BCT ceramic.

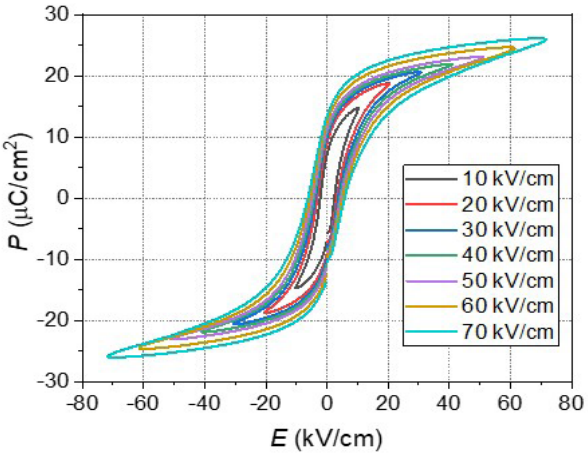

Figure 4: Polarization - electric field- loops of BZT-BCT ceramic measured at 50 Hz and room temperature.

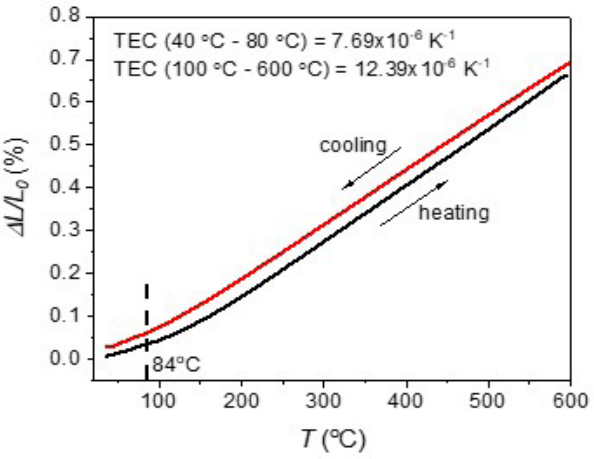

Figure 5: The linear thermal expansion of BZT-BCT ceramic measured between room temperature and 600 °C. The inflexion point and TEC were determined from the cooling curve.

4 Conclusions

In conclusion, this study focused on determining the thermal expansion behavior of $0.5Ba(Zr_{0.2}Ti_{0.8})O_3$-$05(Ba_{0.7}Ca_{0.3})TiO_3$ (BZT-BCT) bulk ceramic. The powder, prepared by solid-state synthesis, was compacted and sintered to a high relative density at 1450 °C for 4 hours. The ceramic crystallized in the perovskite phase. The microstructure consisted of about 10 μm sized grains. The measurement of the dielectric permittivity versus temperature revealed two anomalies which could be related to the phase transitions of the predominantly rhombohedral to tetragonal phase at about 40 °C and to cubic phase at about 90 °C. The hysteretic dependence of the polarization versus the electric field confirmed the ferroelectric nature of the ceramic. The dilatometric measurements revealed the thermal expansion coefficients of the polar and cubic phases of 7.69×10^{-6} K^{-1} (40 °C – 80 °C) and 12.39×10^{-6} K^{-1} (100 °C – 600 °C). The study results contribute to the design of thick and thin-film structures based on BZT-BCT in various energy-harvesting and/or energy-storage applications.

5 Acknowledgments

The authors acknowledge the advice and technical support of Silvo Drnovšek, Electronic Ceramics Department, Jožef Stefan Institute.

6 Conflict of interest

The authors declare no conflict of interest.

The authors acknowledge the financial support of the Slovenian Research Agency (core funding P2-0105).

7 References

1. W. Liu and X. Ren, "Large piezoelectric effect in Pb-free ceramics," *Phys Rev Lett*, vol. 103, no. 25, 257602, Dec. 2009, https://doi.org/10.1103/PhysRevLett.103.257602.
2. M. Acosta, N. Novak, W. Jo, and J. Rödel, "Relationship between electromechanical properties and phase diagram in the $Ba(Zr_{0.2}Ti_{0.8})O_3$-x $(Ba_{0.7}Ca_{0.3})TiO_3$ lead-free piezoceramic," *Acta Mater*, vol. 80, pp. 48–55, 2014, https://doi.org/10.1016/j.actamat.2014.07.058.
3. J. Rödel, K. G. Webber, R. Dittmer, W. Jo, M. Kimura, and D. Damjanovic, "Transferring lead-free piezoelectric ceramics into application," *J Eur Ceram Soc*, vol. 35, no. 6, pp. 1659–1681, Jun. 2015, https://doi.org/10.1016/j.jeurceramsoc.2014.12.013.
4. X. Yan *et al.*, "Correspondence: Lead-free intravascular ultrasound transducer using BZT-50BCT ceramics," *IEEE Trans Ultrason Ferroelectr Freq Control*, vol. 60, no. 6, pp. 1272–1276, 2013, https://doi.org/10.1109/TUFFC.2013.2692.
5. K. K. Poon, M. C. Wurm, D. M. Evans, M. Einarsrud, R. Lutz, and J. Glaum, "Biocompatibility of (Ba,Ca)$(Zr,Ti)O_3$ piezoelectric ceramics for bone replacement materials," *J Biomed Mater Res B Appl Biomater*, vol. 108, no. 4, pp. 1295–1303, May 2020, https://doi.org/10.1002/jbm.b.34477.
6. C. S. Manohar *et al.*, "Novel Lead-free biocompatible piezoelectric Hydroxyapatite (HA) – BCZT $(Ba_{0.85}Ca_{0.15}Zr_{0.1}Ti_{0.9}O_3)$ nanocrystal composites for bone regeneration," *Nanotechnol Rev*, vol. 8, no. 1, pp. 61–78, May 2019, https://doi.org/10.1515/ntrev-2019-0006.
7. "DIRECTIVE 2002/95/EC OF THE EUROPEAN PARLIAMENT AND OF THE COUNCIL of 27 January 2003 on the restriction of the use of certain hazardous substances in electrical and electronic equipment."
8. "JIS-C-0950: 2005 (E), 'The marking for presence of the specific chemical substances for electrical and electronic equipment', Japanese Standards Association, 2005".
9. L. M. Benson and K. K. Reczek, "A guide to United States electrical and electronic equipment compliance requirements," Jun. 2021. https://doi.org/10.6028/NIST.IR.8118r2.
10. V. S. Puli *et al.*, "Structure, dielectric, ferroelectric, and energy density properties of (1 – x)BZT–xBCT ceramic capacitors for energy storage applications," *J Mater Sci*, vol. 48, no. 5, pp. 2151–2157, Mar. 2013, https://doi.org/10.1007/s10853-012-6990-1.
11. Neha, R. Pandey, M. Bhatnagar, P. Kumar, R. K. Malik, and C. Prakash, "Improved dielectric and energy storage properties in $(1\text{-}x)BaTi_{0.80}Zr_{0.20}O_3$-$xBa_{0.70}Ca_{0.30}Ti_{0.99}Fe_{0.01}O_3$ ceramics near morphotropic phase boundary," *Mater Lett*, vol. 318, 132126, Jul. 2022, https://doi.org/10.1016/j.matlet.2022.132126.
12. M. Acosta, N. Novak, G. A. Rossetti, and J. Rödel, "Mechanisms of electromechanical response in (1 - X)$Ba(Zr_{0.2}Ti_{0.8})O_3$-x$(Ba_{0.7}Ca_{0.3})TiO_3$ ceramics," *Appl Phys Lett*, vol. 107, no. 14, 142906, Oct. 2015, https://doi.org/10.1063/1.4932654.
13. D. S. Keeble, F. Benabdallah, P. A. Thomas, M. Maglione, and J. Kreisel, "Revised structural phase diagram of $(Ba_{0.7}Ca_{0.3}TiO_3)$-$(BaZr_{0.2}Ti_{0.8}O_3)$," *Appl Phys Lett*, vol. 102, no. 9, 092903, Mar. 2013, https://doi.org/10.1063/1.4793400.

14. J. Hao, W. Bai, W. Li, and J. Zhai, "Correlation between the microstructure and electrical properties in high-performance $(Ba_{0.85}Ca_{0.15})(Zr_{0.1}Ti_{0.9})O_3$ lead-free piezoelectric ceramics," *Journal of the American Ceramic Society*, vol. 95, no. 6, pp. 1998–2006, Jun. 2012, https://doi.org/10.1111/j.1551-2916.2012.05146.x.
15. L. Song, S. Glinsek, S. Drnovsek, V. Kovacova, B. Malic, and E. Defay, "Piezoelectric thick film for power-efficient haptic actuator," *Appl Phys Lett*, vol. 121, no. 21, 212901, Nov. 2022, https://doi.org/10.1063/5.0106174.
16. P. Muralt, "Polar oxide thin films for MEMS applications," T. Schneller, R. Waser, M. Kosec and D. Payne (Eds.), *Chemical Solution Deposition of Functional Oxide Thin Films, Wien, Austria, Springer-Verlag, 2013, Ch. 24, pp. 593-620*. https://doi.org/10.1007/978-3-211-99311-8_24.
17. T. A. Berfield, R. J. Ong, D. A. Payne, and N. R. Sottos, "Residual stress effects on piezoelectric response of sol-gel derived lead zirconate titanate thin films," *J Appl Phys*, vol. 101, no. 2, 024102, Jan. 2007, https://doi.org/10.1063/1.2422778.
18. L. Lian and N. R. Sottos, "Effects of thickness on the piezoelectric and dielectric properties of lead zirconate titanate thin films," *J Appl Phys*, vol. 87, no. 8, pp. 3941–3949, Apr. 2000, https://doi.org/10.1063/1.372439.
19. K. Coleman, J. Walker, T. Beechem, and S. Trolier-McKinstry, "Effect of stresses on the dielectric and piezoelectric properties of $Pb(Zr_{0.52}Ti_{0.48})O_3$ thin films," *J Appl Phys*, vol. 126, no. 3, 034101, Jul. 2019, https://doi.org/10.1063/1.5095765.
20. R. K. BORDIA and R. RAJ, "Sintering Behavior of Ceramic Films Constrained by a Rigid Substrate," *Journal of the American Ceramic Society*, vol. 68, no. 6, pp. 287–292, Jun. 1985, https://doi.org/10.1111/j.1151-2916.1985.tb15227.x.
21. A. M. Pashaev, A. Kh. Dzhanakhmedov, and A. A. Aliyev, "Effect of Tensile Stresses on the Breakdown Voltage of Thin Films," *Technical Physics*, vol. 65, no. 1, pp. 54–56, Jan. 2020, https://doi.org/10.1134/S1063784220010211.
22. Y.-N. Bie *et al.*, "Effect of Source Field Plate Cracks on the Electrical Performance of AlGaN/GaN HEMT Devices," *Crystals (Basel)*, vol. 12, no. 9, 1195, Aug. 2022, https://doi.org/10.3390/cryst12091195.
23. Y. Tian *et al.*, "Diversiform electrical and thermal expansion properties of $(1-x)Ba_{0.95}Ca_{0.05}Ti_{0.94}Zr_{0.06}O_3$–(x)Dy lead-free piezoelectric ceramics influenced by defect complexes," *J Mater Sci*, vol. 53, no. 16, pp. 11228–11241, Aug. 2018, https://doi.org/10.1007/s10853-018-2428-8.
24. Y. Tian *et al.*, "Electrical Properties and Thermal Expansion Characteristics of $(1-x)Ba_{0.948}Ca_{0.05}Er_{0.002}Ti_{0.94}Zr_{0.06}O_3$–(x)Pr Lead-Free Piezoelectric Ceramics Sintered at a Low-Temperature," *physica status solidi (a)*, vol. 216, no. 2, 1800622, Jan. 2019, https://doi.org/10.1002/pssa.201800622.
25. Y. Tian *et al.*, "Temperature-dependent ferroelectric and piezoelectric response of Yb^{3+} and Tm3+ co-doped $Ba_{0.95}Ca_{0.05}Ti_{0.90}Zr_{0.10}O_3$ lead-free ceramic," *Journal of Ceramic Processing Research*, vol. 23, no. 4, pp. 430–435, Aug. 2022, https://doi.org/10.36410/jcpr.2022.23.4.430.
26. Y. Tian *et al.*, "Piezoelectricity and Thermophysical Properties of $Ba_{0.90}Ca_{0.10}Ti_{0.96}Zr_{0.04}O_3$ Ceramics Modified with Amphoteric Nd3+ and Y3+ Dopants," *Materials*, vol. 16, no. 6, 2369, Mar. 2023, https://doi.org/10.3390/ma16062369.
27. F. Benabdallah *et al.*, "Structure–microstructure–property relationships in lead-free BCTZ piezoceramics processed by conventional sintering and spark plasma sintering," *J Eur Ceram Soc*, vol. 35, no. 15, pp. 4153–4161, Dec. 2015, https://doi.org/10.1016/j.jeurceramsoc.2015.06.030.
28. H. Amorín *et al.*, "Insights into the Early Size Effects of Lead-Free Piezoelectric $Ba_{0.85}Ca_{0.15}Zr_{0.1}Ti_{0.9}O_3$," *Adv Electron Mater*, https://doi.org/10.1002/aelm.202300556.
29. S. López-Blanco, D. A. Ochoa, H. Amorín, A. Castro, M. Algueró, and J. E. García, "Fine-grained high-performance $Ba_{0.85}Ca_{0.15}Zr_{0.1}Ti_{0.9}O_3$ piezoceramics obtained by current-controlled flash sintering of nanopowders," *J Eur Ceram Soc*, vol. 43, no. 16, pp. 7440–7445, Dec. 2023, https://doi.org/10.1016/j.jeurceramsoc.2023.08.012.
30. G. Shirane and A. Takeda, "Volume Change at Three Transitions in $BaTiO_3$ Ceramics," *J Physical Soc Japan*, vol. 6, no. 2, pp. 128–129, Mar. 1951, https://doi.org/10.1143/JPSJ.6.128.
31. Y. Tian *et al.*, "Diversiform electrical and thermal expansion properties of $(1-x)Ba_{0.95}Ca_{0.05}Ti_{0.94}Zr_{0.06}O_3$–(x)Dy lead-free piezoelectric ceramics influenced by defect complexes," *J Mater Sci*, vol. 53, no. 16, pp. 11228–11241, Aug. 2018, https://doi.org/10.1007/s10853-018-2428-8.
32. Y. Tian *et al.*, "Temperature-dependent ferroelectric and piezoelectric response of Yb^{3+} and Tm^{3+} co-doped $Ba_{0.95}Ca_{0.05}Ti_{0.90}Zr_{0.10}O_3$ lead-free ceramic," *Journal of Ceramic Processing Research*, vol. 23, no. 4, pp. 430–435, Aug. 2022, https://doi.org/10.36410/jcpr.2022.23.4.430.

Copyright © 2023 by the Authors. This is an open access article distributed under the Creative Commons Attribution (CC BY) License (https://creativecommons.org/licenses/by/4.0/), which permits unrestricted use, distribution, and reproduction in any medium, provided the original work is properly cited.

Arrived: 09. 01. 2024
Accepted: 13. 02. 2024

Review scientific paper
https://doi.org/10.33180/InfMIDEM2023.404

Informacije MIDEM
Journal of Microelectronics,
Electronic Components and Materials
Vol. 53, No. 4(2023), 239 – 248

Centimeter positioning accuracy in modern wireless cellular networks – wish or reality?

Tomi Mlinar, Sašo Tomažič, Boštjan Batagelj

ICT Department, Faculty of Electrical Engineering, University of Ljubljana, Slovenia

Abstract: The paper explores the evolution of wireless positioning technologies across cellular network generations, emphasizing the advancements from 2G to the current 5G and anticipating the upcoming 6G around 2030. Positioning methods, such as Theta-Theta, Rho-Rho, and Hyperbolic, are discussed for both two-dimensional and three-dimensional applications, revealing the complexities and improvements in accuracy. The limitations of methods like Theta-Theta are addressed, and enhancements through multi-antenna systems are explored. The role of Ultra-Wideband (UWB) technology in overcoming the limitations of Received Signal Strength Measurement (RSSI) for accurate distance measurements is highlighted. The abstract underscores the continuous strive for precision in location determination, catering to diverse applications from industrial automation to sports and rehabilitation.

Keywords: positioning, wireless systems, positioning accuracy, 2G, 4G, 5G, 6G

Centimetrska natančnost pozicioniranja v sodobnih brezžičnih celičnih omrežjih – želja ali resničnost?

Izvleček: Ta članek opisuje metode, ki se uporabljajo v brezžičnih celičnih omrežjih za določanje položaja terminala ali druge brezžične naprave. Članek obravnava metode in njihovo natančnost pri določanju lokacije. Vse generacije celičnih omrežij, od druge generacije (2G) naprej, imajo vgrajene mehanizme za določanje položaja uporabnika. Natančnost se je z razvojem generacij povečevala in se pričakuje, da bo dosegla centimetrsko natančnost v šesti generaciji. Določene industrije, kot so zdravstvo in industrijska proizvodnja, zahtevajo še posebej natančno določitev položaja, zato je za sodobna celična omrežja ključno, da to omogočajo na cenovno ugoden, energetsko učinkovit, zanesljiv in varen način. Pomembno je, da so te storitve zagotovljene predvsem znotraj stavb. Rezultati naše raziskave kažejo, da sta peta (5G) in šesta (6G) generacija zelo blizu izpolnitvi omenjenega merila centimetrske natančnosti pri določanju položaja.

Ključne besede: pozicioniranje, brezžični sistemi, centimetrska natančnost, 2G, 4G, 5G, 6G

** Corresponding Author's e-mail: tomi.mlinar@fe.uni-lj.si, bostjan.batagelj@fe.uni-lj.si*

1 Introduction

The pursuit of highly accurate location systems has become an integral part of modern society, where location-based services are ubiquitous and essential for numerous applications, from navigation and emergency response to asset tracking and virtual reality (VR) / augmented reality (AR) / extended reality (XR). High positioning accuracy is of utmost importance in many of the industries listed in Table 1.

Wireless cellular networks have long been seen as a promising platform for precise location capabilities. Even the second generation (2G) wireless systems enabled identification, which determined the terminal's position according to the coverage of an individual sector of the base station. This worked everywhere, but the accuracy depended on the size of the cell and/or sector. However, achieving centimeter-level accuracy in such networks is not a trivial task, as it involves overcoming

How to cite:
T. Mlinar et al., "Centimeter positioning accuracy in modern wireless cellular networks – wish or reality?", Inf. Midem-J. Microelectron. Electron. Compon. Mater., Vol. 53, No. 3(2023), pp. 239–248

© MIDEM Society

a variety of technological challenges and reconciling different factors that affect localization accuracy. Better accuracy can already be obtained by measuring the strength of the received power, but we must know the signal losses on the radio path. From this, we can estimate the terminal's distance from nearby base stations and then determine its position using the intersections of the virtual circles formed around the base stations by the calculated distance values. Since the strength of the received power depends on the orientation of the user's device and the environment in which the user is located, the accuracy is good only when the user is in the direct line of sight or near the base station. In modern cellular networks with enough bandwidth (5G and 6G) we can expect to determine the position of any object very precisely, even with centimeter accuracy [1]. Centimeter-level accuracy will be of utmost importance in industries such as healthcare and manufacturing, as well as logistics, sports and gaming.

Table 1: Industries and value of accurate positioning.

Industry	Value of positioning
Military and defense	• Locating people • Unmanned aerial vehicle (UAV) navigation • Unmanned underwater vehicles (UUV) navigation • Robot navigation
Healthcare management, hospitals, and clinics	• Locating patients and visitors • Tracking medical equipment
Warehousing, logistics and distribution	• Product inventory • Collision avoidance and maritime precise docking • Optimizing routes
Manufacturing	• Managing inventory • Optimizing workflow • Quality assurance
Sports, entertainment, and gaming	• Enhanced analytics • Improving player performance • Location aware apps (VR/AR/XR)

The remainder of this scientific paper is structured as follows: The next section gives a basic understanding of cellular networks. Then, we dive into the details of how accurately devices can be located within these networks. Here, we explore the current state-of-the-art methodologies, technological advances, and potential ways to bridge the gap between wishful thinking and practical reality. Additionally, we scrutinize the limitations of conventional positioning approaches based on measurements of signal strength, time-of-arrival, and angle-of-arrival. What follows is a discussion on positioning in 5G, driven by the escalating demand for improved accuracy and the significant pressure on the wireless industry to develop innovative solutions that meet these expectations. The fifth section is dedicated to positioning accuracy and the extent of uncertainty, expressed as an area. In conclusion, this scientific inquiry not only illuminates the theoretical aspects of achieving centimeter-level positioning accuracy in wireless cellular networks but also provides valuable insights into the practical feasibility and real-world challenges that lie ahead. By presenting a comprehensive overview of the current situation, this paper aims to foster dialogue and collaboration among researchers, industry representatives, and policymakers to turn the aspiration of centimeter-level positioning in wireless cellular networks into a tangible reality.

2 Cellular networks

In the second generation (2G), a simple time measurement method has been used for decades. The principle behind this method is that the base station sends a command to the terminal. Based on the response, it sets the corresponding time delay of the signal. This functionality basically enabled normal communication between the base station and fast-moving terminals, but the position accuracy was inaccurate. Therefore, the extended Cell ID was introduced for the location-based emergency call service [2]. In 2G networks, time was typically measured with a resolution of about 4.615 µs and an uncertainty or margin of error of around ±20 µs.

In the fifth generation (5G), we expect to be able to determine the position of the terminal with an accuracy of better than one metre. New technical solutions are used, e.g. determining the angle of transmission and reception, measuring the signal propagation time across several cells and measuring the time difference when user devices only receive signals. The latter is typical for satellite navigation. It enables the terminal to determine its position without the network knowing about it, as an terminal does not utilise network resources [3], [4]. In addition to broadband mobility [5], increased responsiveness, constant availability, enhanced security and other improvements, 5G, which meets the capacity requirements of modern applications, will also bring more accurate determination of the position of wireless devices. The 5G is unlikely to deliver everything we expect of it, especially when deployed in a non-standalone mode of operation [6].

Much of what is promised in 5G - including position accuracy of a few centimeters - will probably be delivered by the sixth generation (6G). The following enhancements in 6G may contribute to the expected accuracy of around one centimeter:

- Densification of base stations and antennas allows more precise triangulation and localization of devices.
- Technologies such as massive MIMO (Multiple Input Multiple Output) and beamforming improve signal strength and directionality, enhancing the accuracy of location estimation.
- Integration of edge computing capabilities enables faster data processing closer to the source (at the network edge). This facilitates real-time data analysis and decision-making, leading to more accurate localization results.
- 6G networks may use artificial intelligence and machine learning algorithms to analyze large amounts of data and optimize localization algorithms. AI can learn from patterns and improve the accuracy of location estimation over time.

The 6G, designed to be superior to previous generations in all parameters, will be used in the fight against modern challenges facing humanity, such as epidemics and natural disasters, allowing us to monitor people's movements and save lives without violating their privacy. Tracking is one of the most important features of modern wireless cellular networks and opens many use cases in the field of digitalisation. With digitalisation, the industry is also striving for automated production processes and mobile robots with centimeter-accurate positioning, especially indoors where global satellite navigation systems do not work [7]. In sport and rehabilitation, knowledge of posture in combination with biomechanical feedback [8] helps to promote the athlete's motor skills and monitor their training.

3 Positioning methods

Modern localisation methods use electronic devices, which are an example of complex and sophisticated high-frequency technology in engineering. These procedures are essentially based on a system of high-frequency electromagnetic beacons distributed in space. By processing signals from these beacons and knowing their positions, the receiving device can determine its position with a certain degree of accuracy. In doing so, it employs two-dimensional positioning through one of the following geometric methods [9]:

- Theta-Theta (with two azimuths),
- Rho-Rho (with two distances),
- Rho-Theta (with distance and azimuth),
- Hyperbolic (with distance differences of up to three beacons).

The methods mentioned above are applicable for determining the position of an object in two dimensions. For three-dimensional positioning, a minimum of four beacons must be available.

The 3rd Generation Partnership Project (3GPP) committee identified positioning methods in 3GPP Releases 15, 16, and 17, all related to power, angular, or time measurements. 5G indoor positioning in offices, shops, etc., is specified in 3GPP Release 16, with certain enhancements for industrial applications (e.g., manufacturing, logistics) in 3GPP Release 17. Combining 5G and the Satellite Navigation System (GNSS) can achieve a positioning accuracy of ten meters outdoors or in rural and urban clear sky areas.

Positioning methods in 4G (3GPP Release 15) use the following mechanisms:

- Observed Time Difference of Arrival (OTDoA),
- Uplink Time Difference of Arrival (UL-TDoA),
- Positioning methods based on power measurements (RSS).

In 5G, the list of aforementioned mechanisms is expanded by two more (3GPP Release 16 and 17), namely:

- Round trip time (RTT),
- Angle of Arrival/Angle of Departure (AoA/AoD).

3.1 Theta-Theta Method

In the Theta-Theta system (positioning with two azimuths), as illustrated in Figure 1, a terminal at an unknown location measures the angle between the reference direction determined by north and the orientation towards two or more base stations with known locations. By utilizing the measured angles, the termi-

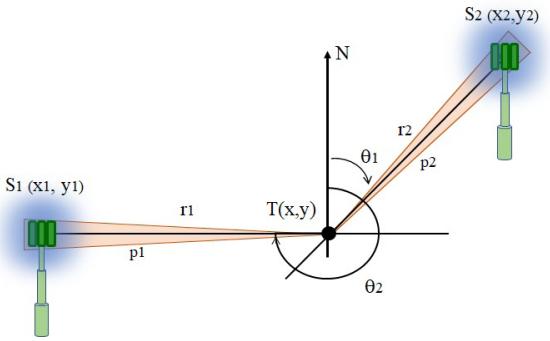

Figure 1: Positioning with the Theta-Theta system: the terminal measures the azimuth angle θ - between the reference direction determined by north - and the orientation to two or more base stations at an unknown location.

nal determines its position at the intersection of the lines.

The terminal position T (x, y) is calculated from equation (1):

$$y = \frac{y_2 \cdot \tan(\theta_2) - x_2}{\tan(\theta_2) - \tan(\theta_1)}, \; x = y \cdot \tan(\theta_1) \tag{1}$$

This system is not very accurate due to the imprecision in angle measurements. The error is proportional to the distance between the terminal and the beacon, which can be calculated using equation (2):

$$\Delta P = r \cdot \sin(\Delta\alpha) = r \cdot \Delta\alpha \tag{2}$$

where ΔP is the positioning error, r is the distance between the terminal and the base station (beacon), and Δα is the angle measurement uncertainty. If lines p1 and p2 in Figure 1 intersect perpendicularly, the error area is the smallest. Therefore, it makes sense to choose base stations that are perpendicular to each other in relation to the user's position. As already mentioned, the positioning error of the Theta-Theta system increases proportionally to the distance of the terminal from the base station(s). For example, with an angular uncertainty of ±1 degree at a 100 m distance from the base station, using equation (2), the positioning error is 1.7 meters. If the distance of the terminal from the base station increases by a factor of ten, the error also increases by a factor of ten, reaching 17 meters.

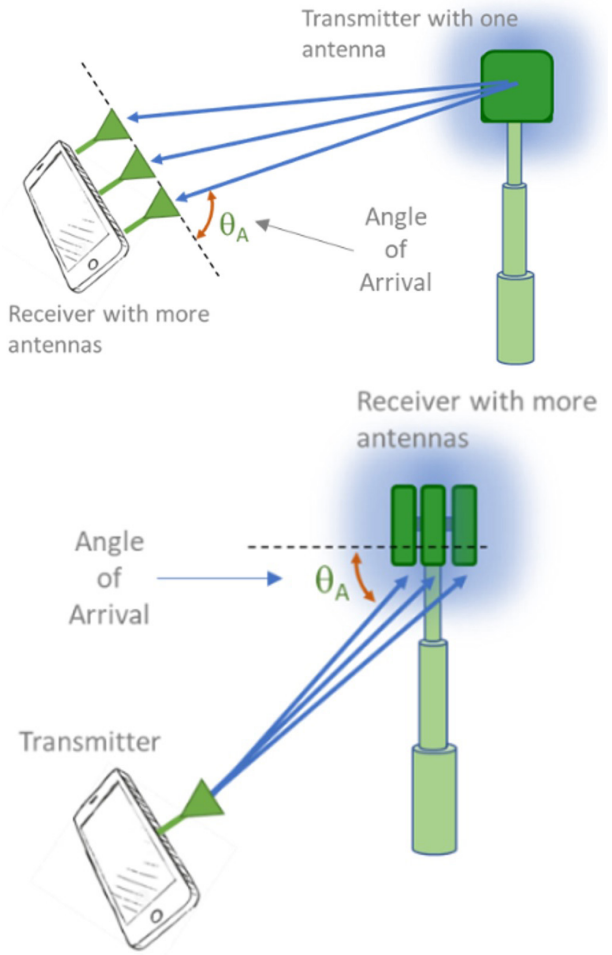

Figure 2: Multiple antennas on the receiver side enable AoA measurements.

To determine the angle at which the terminal receives the beacon signals, i.e. the angle of arrival, a system with several antennas is used, where multiple antennas can be on the receiving side (Figure 2) or on the transmitting side (Figure 3).

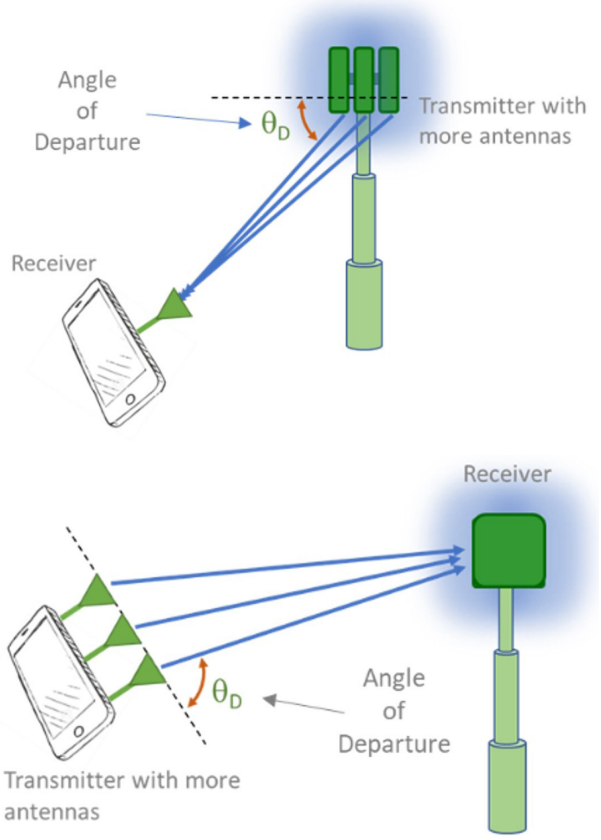

Figure 3: Multiple antennas on the transmitter side enable AoD measurements.

In a multi-antenna system on the receiving side (Figure 2), the angles of arrival (AoA) are measured. Each antenna receives a signal with a different phase, allowing the calculation of the antenna's direction. In the case of a system with several antennas on the transmitting side (Figure 3), the angles of departure (AoD) are measured. Each antenna transmits at its own time, and the receiver receives signals with different phases, enabling the calculation of the transmission angle. In both cases, AoA and AoD, the angle can be calculated from

the measured phase difference of the signals arriving at the pair of receiving antennas, as illustrated in Figure 4.

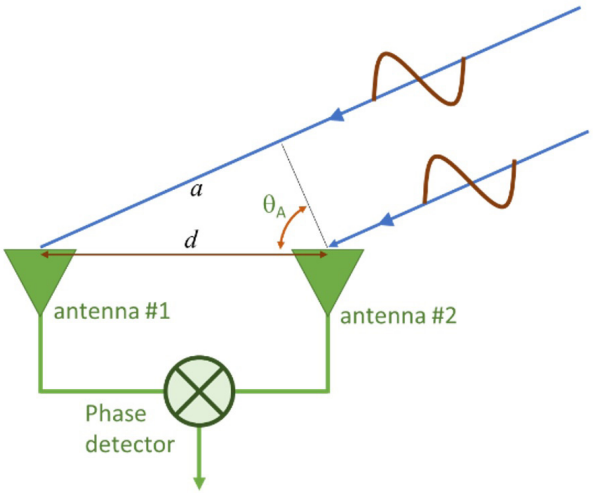

Figure 4: Positioning with the Theta-Theta system.

The phase difference φ is calculated according to equation (3):

$$\varphi = \frac{a}{\lambda} \cdot 2\pi = \frac{d}{\lambda} \cdot 2\pi \cdot \sin\theta_A \tag{3}$$

The angle of arrival θ_A, at which the signals arrive, depends on the distance d between the receiving antennas, the wavelength λ of the signal, and the measured phase difference ϕ. The angle of arrival is calculated according to equation (4):

$$\theta_A = arc\sin\frac{\phi\lambda}{2\pi d} \tag{4}$$

Beam shaping by adjusting the phase difference between the antennas [7] is more effective in the millimeter wave part of the spectrum, where optical technologies are used for better accuracy [8].

The Theta-Theta method is rarely used in its version based only on basic geometrical laws and phase measurements. However, with the use of additional mechanisms enabled by modern cellular networks, this method becomes very accurate.

3.2 Rho-Rho Method

In the Rho-Rho system (positioning of the terminal with two known distances), the terminal at an unknown location measures the distance between it and two or more base stations with known locations (Figure 5). The terminal position T (x, y) is calculated from equation (5):

$$\rho_1^2 = x^2 + y^2$$
$$\rho_2^2 = (x - x_2)^2 + (y - y_2)^2 \tag{5}$$

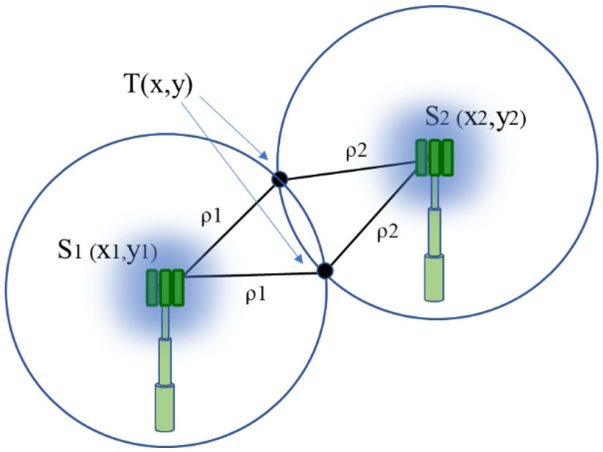

Figure 5: Positioning the terminal with the Rho-Rho system: the distance between the terminal at an unknown location and two or more base stations at known locations is measured.

The terminal determines its location using the trilateration process, based on the intersections of virtual circles formed by the distance, calculated from the travel time measurements from the base station to the terminal. The terminal's position is defined as the intersection of two circles, each with a base station at the center. The uncertainty of the travelling time refers to non-ideal measurements, so the distance from the terminal represents a ring and not a circle, and the result is that the intersection of the rings in Figure 6 is a green uncertainty region.

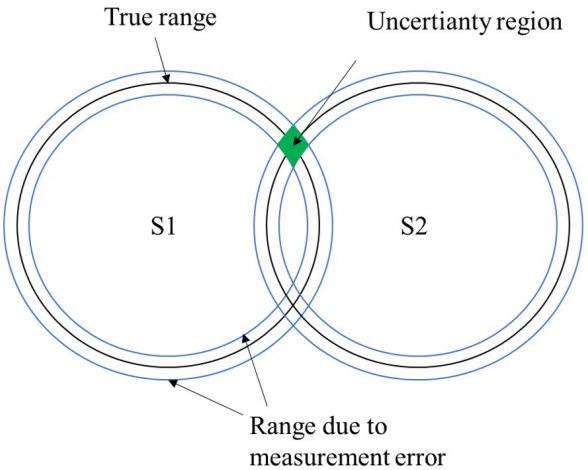

Figure 6: Uncertainty region (depicted by the green patch) in the Rho-Rho positioning system.

The size and shape of the uncertainty region depends on the distance between the centres of the rings and

their thicknesses. Another weakness is that the intersection of two rings results two solutions, introducing ambiguity. This can be resolved by measuring the distance from a third base station (e.g. from RSSI data, see section 3.5) or by knowing the previous position of terminal, which is likely close to the current position.

3.3 Rho-Theta Method

In the Rho-Theta system (positioning of the terminal with a known distance and angle), the terminal measures the distance to the base station and its azimuth (Figure 7). The terminal position T (x, y) is calculated from equation (6):

$$x = \rho \cdot sin(\theta)$$
$$y = \rho \cdot cos(\theta). \quad (6)$$

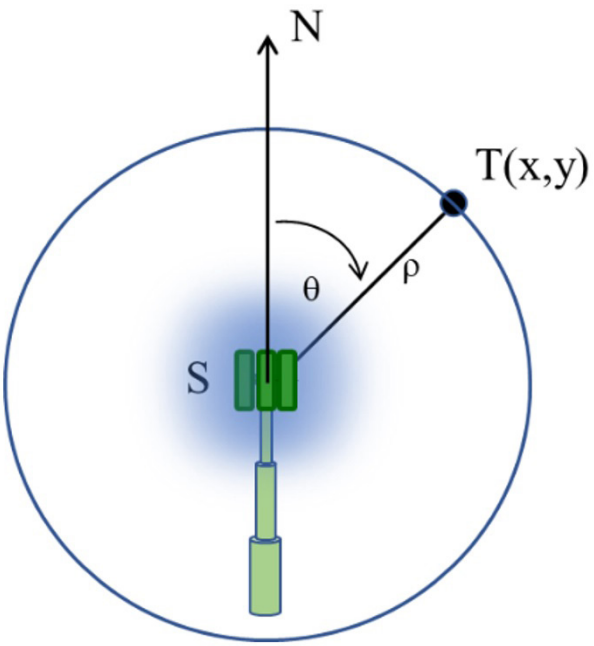

Figure 7: Positioning with the Rho-Theta system involves the terminal at position T(x, y) measuring the distance to the base station and its azimuth.

3.4 Hyperbolic Method

In the Hyperbolic system, a terminal at an unknown location measures the time differences between itself and two base stations at known locations. A 5G receiver only computes its position based on the relative time of the individual base stations, which is known as the Downlink Time Difference of Arrival (DLTDOA). In 4G, this function is referred to as observed time difference of arrival (OTDOA) [12], described in the 3GPP Release 15 specifications. In both cases, the time difference of the base stations is measured, but they must all be ynchronized. The user terminal, in this case, functions similarly to a satellite navigation signal receiver. For this purpose, base stations transmit a positioning reference signal (PRS). The accuracy of the calculation of the terminal's position depends on the synchronization and measurement of time differences. The hyperbolic method for determining position has been used for years by maritime systems (e.g. LORAN, now e-LORAN) and satellite navigation systems such as GPS, GLONASS, Galileo, Beidou and others.

3.5 Received Signal Strength Measurement

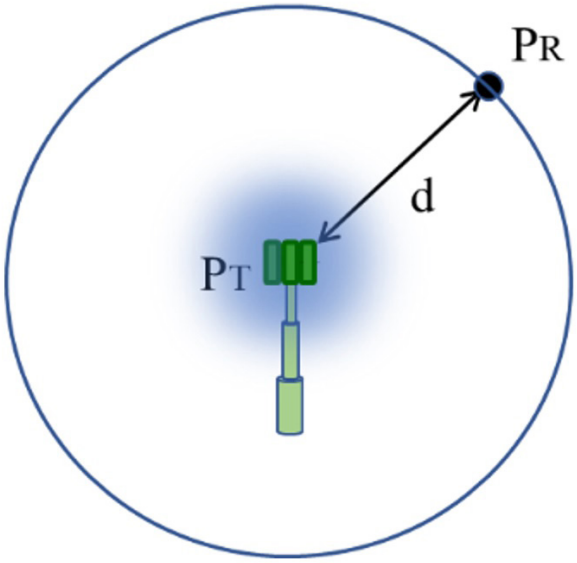

Figure 8: Received Signal Strength measurements. The terminal calculates the distance to the base station from the RSSI indicator.

Ideally, we can determine the power of the received signal using equation (7):

$$P_R = \frac{P_T \cdot G_T \cdot G_R \lambda^2}{(4\pi d)^2} \quad (7)$$

d is the distance between the transmitter (P_T, G_T) and receiver (P_R, G_R), and λ is the wavelength of the signal.

Using the Received Signal Strength Indicator (RSSI) to determine position is simple and requires only negligible additional costs. The measurement is independent of the modulation process and data transfer rate and does not require synchronization between devices. It works best near the base station, as accuracy depends on distance and environment, as shown in Figure 9.

Since it is not possible to know signal losses on the radio path in a dynamic mobile environment, and the measurement result is also affected by the orientation of the user device, a comparison with a pre-made learning da-

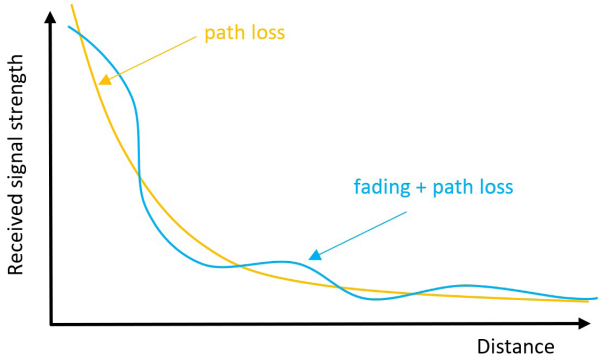

Figure 9: The problem of positioning from the measured received power depends on the distance from the base station and the environment.

tabase is useful [13]. The RSSI at a distance d from the transmitter is calculated according to equation (8):

$$RSSI_d = -10 \cdot n \cdot \log_{10}(d) + RSSI_0 \quad (8)$$

$RSSI_0$ is constant, index n represents losses in space and depends on environment (Table 2).

Table 2: Index *n* in different environments [10].

Environment	Environment index (n)
Free space	2
Metropolitan area	3 – 5
Office building	4 – 6
Factory	2 – 3

Distance measurement is enhanced through indirect means, particularly by measuring time. 3GPP Release 8 introduced cell identification, present in all cellular network generations, with accuracy dependent on cell or sector size. In 4G, Timing Advance improved cell identification by adjusting the expected time delay for receiving the terminal's signal. 5G introduced a multi-cell Round-Trip Time (RTT) measurement function, enabling the terminal to determine distances without time synchronization. The RTT value, representing the time each frame travels from the transmitter to the receiver and back, is used to calculate distances to individual 5G base stations (gNBs). Taking into account signal processing time, the distance (d) between the transmitter and the receiver is calculated using the speed of light (c) in equation (9):

$$d = \frac{RTT}{2} \cdot c \quad (9)$$

However, due to factors affecting the accuracy of RSSI determination, such as antenna patterns, reflections, and obstacles, RSSI alone is rarely used for precise distance measurements and positioning.

For more accurate time measurements, a signal with the largest possible bandwidth is required. This is an advantage of ultra-wideband radio communication systems (UWB). Modern mobile networks provide sufficient radio spectrum, facilitating more precise time measurements and, consequently, more accurate positioning.

4 Positioning in 5G

The positioning method in 5G, defined in 3GPP Release 15, is known as Observed Time Difference of Arrival (OTDOA). Certain conditions must be met for this method: The base stations (gNBs) must be synchronised, the positions of the gNBs must be known, and at least three beacons are required. The position is calculated by the receivers of the gNBs. In this scenario, 5G terminals are passive, as they only receive signals, similar to satellite navigation terminals.

As far as time and angle-based positioning methods are concerned, 5G introduces several improved parameters for better accuracy. The delay error variance decreases in the order of the square of the bandwidth as the bandwidth increases. Angle variance remains completely independent of the bandwidth. 5G offers a significant improvement in bandwidth compared to LTE (20 MHz for 4G compared to 100 to 400 MHz for 5G). Received power is inversely proportional to all estimation variances and can be increased by beamforming. 5G provides five different choices for subcarrier spacing (15 kHz, 30 kHz, 60 kHz, 120 kHz, and 240 kHz). The subcarrier spacing linearly increases the angle variance and simultaneously linearly decreases the delay variance. To counteract this effect, increasing the receiving power is a natural solution.

Different antenna patterns (varied spacings and the number of polarisations in the antenna array) do not affect the delay variance but rather the total number of antenna elements in the array. The number of rows and columns of the antenna array results in a cubic decrease in the angle variances.

In the 5G architecture (3GPP Release 16), specific elements are dedicated to positioning:
The Location Management Function (LMF) receives results of measurements and assistance information from the gNB and the terminal, via the Access and Mobility Management Function (AMF), to compute the position of the terminal.

A new NR Positioning Protocol (NRPPa) is introduced between the radio network and the core network, which carries positioning information between the radio network and the LMF via the Next Generation Control plane (NG-C) interface. The LMF configures the 5G terminal using the LTE Positioning Protocol (LPP).

5G utilizes two reference signals for positioning: the Positioning Reference Signal (PRS) in the downlink and the Sounding Reference Signal (SRS) in the uplink.

Beamforming can be used for more precise positioning, which improves the signal-to-noise ratio by increasing the gain of the beamforming. The terminal position is provided in terms of the Angle of Departure (AoD), while multiple antennas at the gNB in the uplink enable precise Angle of Arrival (AoA) measurements.

Table 3 presents a comparison of the estimated average positioning accuracy of various technologies [7].

Table 3: Positioning accuracy of different technologies.

Technology	Accuracy (m)
4G	20 – 50
5G on cmWaves	10 – 20
5G on mmWaves	<1

5 Positioning accuracy and area of uncertainty

As an illustration of position accuracy determination, we consider the AoA method, which is closely linked to the area of uncertainty. This scenario is depicted in Figure 10 with two base stations (Tx1, Tx2) and a mobile user (Rx).

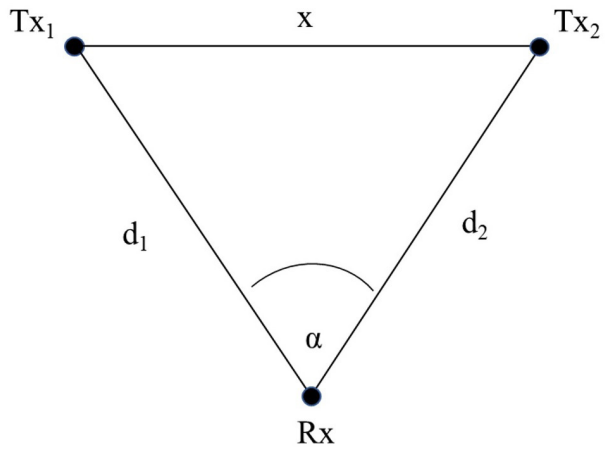

Figure 10: Geometry for determining the position and uncertainty area of the terminal (receiver).

The two stations are separated by a distance x, and the user sees the transmitters at an angle α. We also consider the angle measurement error, denoted by Δ. By changing the angle α, we can observe changes in the size of the uncertainty area. In our example we assume that the distance between the receiver and each transmitter is the same (d1 = d2 = d).

To calculate the distance of the receiver from the transmitters, equation (10) is used. It is consistent with the basic geometry of an isosceles triangle.

$$d = \frac{\frac{x}{2}}{\sin\left(\frac{\alpha}{2}\right)} \tag{10}$$

where d is the distance between the receiver and each transmitter, x is the fixed distance between the transmitters, and α is the angle at which the receiver sees both transmitters. The position error δp is determined by equation (11). The expression can be simplified due to the small value of the error:

$$\delta p = d \cdot \sin\left(2\Delta\right) = d \cdot 2\Delta \tag{11}$$

Finally, we come to the equation (12) for calculation the area of uncertainty.

$$A = \frac{\left(d \cdot 2\Delta\right)^2}{\sin \alpha} \tag{12}$$

The input data for calculating the uncertainty area are as follows: distance between transmitters (x) is 500 m, measurement error (Δ) is ±10 milliradians, and angle (α) is between 1 and 178 degrees. We use the Matlab tool for the calculation. The Figures 11 and 12 show how the uncertainty area varies with angle and distance [16].

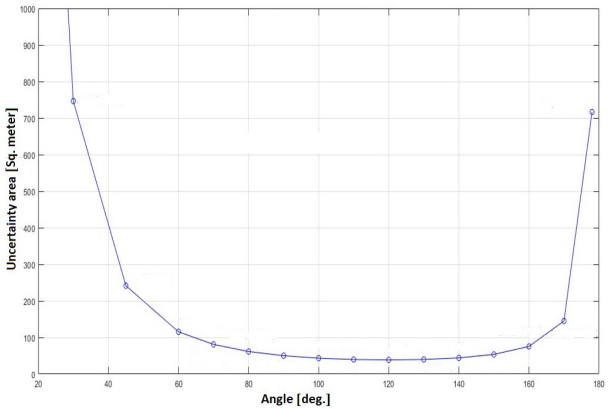

Figure 11: Uncertainty area as a function of angle.

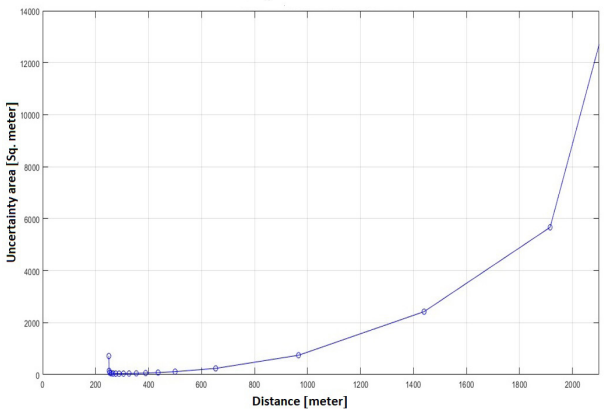

Figure 12: Uncertainty area as a function of distance.

Figure 11 shows that the uncertainty area decreases as the angle increases. In this case, the smallest area of uncertainty is when the angle of arrival is 120 degrees, and the user is at 289 meters. At that point the area of uncertainty is 38.5 m^2 and consequently the most precisely determined location. If the angle approaches zero or 180 degrees, the area increases greatly due to the geometry of the angle and the trigonometric functions, so that these extreme angles are not taken into account in the calculation. We can logically conclude that the measurements become less accurate as the distance between the user and the base stations increases, as it is shown in Figure 12.

6 Results and discussion

We can conclude that centimeter positioning accuracy with cellular technologies is possible inside buildings under certain conditions. This is possible on mmWave frequencies using mechanisms built into modern cellular networks as: Downlink Observed Time Difference of Arrival (DL-TDOA, assisted by the terminal), Uplink Time Difference of Arrival (UL-TDoA, assisted by the base station), and RTT.

Methods used for positioning outside buildings, however, allow the positioning with a few meters' accuracy on cmWave frequencies, which is sufficient for most smart outdoor applications, e.g. smart agriculture, outdoor asset tracking, environment monitoring, smart city infrastructure, outdoor events, and the like. In outdoor cases, for less precise measurements, we can use other previously mentioned methods. In many outdoor cases, a combination of cellular and satellite technologies is very useful, e.g., combination of 5G and GPS.

Finally, the design of the antenna (MIMO or single-beam antenna) and the antenna pattern have a great influence on the accuracy of the position determination. Narrower beamwidth means a higher gain of the antenna, which results in higher received power and higher accuracy in determining the distance. Narrow beamwidth also improves user positioning resolution, reduces the susceptibility to more reflections from the environment and reduces interference. Therefore, MIMO antenna with beamforming [17], [18], offers the positioning accuracy down to sub-meter level, which is much better than a standard single-beam antenna.

7 Conclusions

This paper discusses positioning methods in modern cellular networks that may be suitable for the new challenges brought by the smart industry. When using several base stations, the position can be determined by different signal measurement methods: (a) by measuring the Angle of Arrival (AoA), (b) by measuring the Angle of Departure (AoD), (c) by measuring the Round-Trip Time (RTT), and (d) by measuring the Observed Time Difference of the received signal (OTDoA).

As seen from the example in Chapter 5, the accuracy of position determination is closely related to the size of the uncertainty area. This depends on the angle at which the user sees the base stations and the distance from the base stations. The uncertainty area strongly depends on the triangle geometry of the base stations and the user.

If a single base station is available, we can use the Rho-Theta method, which identifies the distance between the terminal and the base station by measuring the Round-Trip Time (RTT) and the angle by measuring the Angle of Arrival (AoA).

The combination of different methods for determining the position of the terminal and adding new ones to the standards allows for better position accuracy.

We can summarize the findings in a few observations:

(a) the 5G system can perform positioning without user intervention,
(b) all devices receive a positioning service,
(c) the advantage of the large computing capacity is available in the network,
(d) there is low battery consumption of the terminals, and finally
(e) positioning accuracy in 5G can be of the order of centimeters.

8 Acknowledgments

This work was supported by the Slovenian Research Agency under Grants J2-3048, J2-50072 and research core funding No. P2-0246.

9 Conflict of Interest

The authors of this document have no conflicts of interest (COI) in this paper.

10 References

1. C. De Lima, D. Belot, R. Berkvens et al., Convergent Communication, Sensing and Localization in 6G Systems: An Overview of Technologies, Opportunities and Challenges. IEEE Access 2021, 9, 26902–26925.
2. T. Wigren, Adaptive Enhanced Cell ID Fingerprinting Localization by Clustering of Precise Position Measurements, IEEE Transactions on Vehicular Technology, vol. 56, no. 5, pp. 3199-3209, 2007.
3. F. Gustafsson, F. Gunnarsson, Mobile positioning using wireless networks: possibilities and fundamental limitations based on available wireless network measurements, IEEE Signal Processing Magazine, vol. 22, no. 4, pp. 41-53, July 2005, https://doi.org/10.1109/MSP.2005.1458284.
4. A. H. Sayed, A. Tarighat, N. Khajehnouri, Network based wireless location: challenges faced in developing techniques for accurate wireless location information, IEEE Signal Processing Magazine, vol. 22, no. 4, pp. 24-40, July 2005, https://doi.org/10.1109/MSP.2005.1458275.
5. B. Batagelj, Broadband internet is also 5G, Monitor, Year 31, no. 6, pp. 32-34, June 2021, https://www.monitor.si/clanek/sirokopasovni-internet-jetudi-5g/207663/.
6. M. Grebenc, B. Batagelj, Non-standalone 5G network, 25th Seminar on Radio Communications 2022, 2 - 4 February 2022, Ljubljana, http://srk.fe.unilj.si/zborniki/SRK2022.pdf.
7. M. Šelj, Determining the indoor user's location, Diploma thesis, Faculty of Electrical Engineering, University of Ljubljana, 2022 https://repozitorij.unilj.si/IzpisGradiva.php?lang=slv&id=135224. [Accessed: 15-Jul-2022].
8. A. Kos, V. Milutinović, A. Umek, Challenges in wireless communication for connected sensors and wearable devices used in sport biofeedback applications, Future Generation Computer Systems, Year 92, pp. 582-592, 2019, https://doi.org/10.1016/j.future.2018.03.032.
9. B. Batagelj, T. Mlinar, S. Tomažič, Positioning in modern public mobile networks, Proceedings of the 31st International Electrotechnical and Computer Science Conference ERK 2022, pp. 41-44, 19 - 20 September 2022, Portorož, Slovenia, ISSN 2591-0442 (online).
10. P. Ritoša, B. Batagelj, M. Vidmar, Optically steerable antenna array for radio over fibre transmission, Electronics Letters, vol. 41, no. 16, pp. 917-918, Aug. 2005.
11. P. Ritoša, B. Batagelj, Overview of optically driven antenna systems, I. A. Sukhoivanov (Ed.), V. A. Svich (Ed.), Y. Shimaliy (Ed.), Second International Conference on Advanced Optoelectronics and Lasers: proceedings volume, [Bellingham: Society of Photo-Optical Instrumentation Engineers]: = SPIE, 2008. pp. 1-9, ilustr. Proceedings of SPIE, vol. 7009. ISBN 978-0-8194-7219-9. ISSN 0277-786X. http://spie.org/x648.html?product_id=793861.
12. S. Fischer, Observed Time Difference Of Arrival (OTDOA) Positioning in 3GPP LTE, Qualcomm, 2014, https://www.qualcomm.com/media/.
13. N. Wang, W. Li, L. Jiao et al., Orientation and Channel-Independent RF Fingerprinting for 5G IEEE 802.11ad Devices, IEEE Internet of Things Journal, vol. 9, no. 11, pp. 9036-9048, 1 June1, 2022, https://doi.org/10.1109/JIOT.2021.3119319.
14. S. Sadowski, P. Spachos, K. N. Plataniotis, Memoryless Techniques and Wireless Technologies for Indoor Localization With the Internet of Things, IEEE Internet of Things Journal, vol. 7, no. 11, pp. 10996-11005, Nov. 2020, https://doi.org/10.1109/JIOT.2020.2992651.
15. E. Udvary, Photonic Approach to Phased Array Application, Radioengineering, Sept. 2021, Vol. 30, No. 3, pp. 463-469, https://doi.org/10.13164/re.2021.0463.
16. K. Radakovič, Procedures for locating a mobile user in the Fifth-generation network, Diploma thesis, Faculty of Electrical Engineering, University of Ljubljana, 2023.
17. M. W. Numan, M. T. Islam, N. Misran, FPGA-based hardware realization for 4G MIMO wireless systems, Informacije MIDEM, vol. 40, No. 3, pp. 191-199, 2010.
18. B. Batagelj, L. Pavlovič, L. Naglič and S. Tomažič, Convergence of fixed and mobile networks by radio over fibre technology, Informacije MIDEM, vol. 41, No. 2, pp. 144-149, 2011.

Copyright © 2023 by the Authors. This is an open access article distributed under the Creative Commons Attribution (CC BY) License (https://creativecommons.org/licenses/by/4.0/), which permits unrestricted use, distribution, and reproduction in any medium, provided the original work is properly cited.

Arrived: 20. 11. 2023
Accepted: 27. 02. 2024

Informacije MIDEM
Journal of Microelectronics,
Electronic Components and Materials
Vol. 53, No. 4(2023), 249 – 249

MIDEM 2024

59th INTERNATIONAL CONFERENCE ON MICROELECTRONICS, DEVICES AND MATERIALS WITH THE WORKSHOP ON ELECTROMAGNETIC COMPATIBILITY: FROM THEORY TO PRACTICE

October 2nd – October 4th, 2024
Rimske Toplice, Slovenia

Announcement and Call for Papers

Chairs:

Assoc. Prof. Dr. Benjamin Lipovšek
Assoc. Prof. Dr. Marko Jankovec

IMPORTANT DATES

Abstract submission deadline:
May 17, 2024

Acceptance notification:
June 30, 2024

Full paper submission deadline:
August 31, 2024

Invited and accepted papers will be published in the Conference Proceedings.

Detailed and updated information about the MIDEM Conferences, as well as for paper preparation can be found on

http://www.midem-drustvo.si//

MIDEM

GENERAL INFORMATION
The 59th International Conference on Microelectronics, Devices and Materials with the Workshop on Electromagnetic Compatibility: From Theory to Practice continues the successful tradition of annual international conferences organised by the MIDEM Society, the Society for Microelectronics, Electronic Components and Materials. The conference will be held in Rimske Toplice, Slovenia, from **OCTOBER 2nd – 4th, 2024.**

Topics of interest include but are not limited to:
- Electromagnetic compatibility (workshop topic)
- Novel monolithic and hybrid circuit processing techniques,
- New device and circuit design,
- Process and device modelling,
- Semiconductor physics,
- Sensors and actuators,
- Electromechanical devices, microsystems and nanosystems,
- Nanoelectronics,
- Optoelectronics,
- Photovoltaics,
- Electronic materials science and technology,
- New electronic materials and applications,
- Materials characterization techniques,
- Reliability and failure analysis,
- Education in microelectronics, devices and materials.

ORGANIZER:
MIDEM Society - Society for Microelectronics, Electronic Components and Materials, Slovenia

PARTNERS:
UL FE, IJS, IMAPS - Slovenia Chapter, IEEE - Slovenia Section

Boards of MIDEM *Society* | *Organi društva* MIDEM

MIDEM *Executive Board* | *Izvršilni odbor* MIDEM

President of the MIDEM Society | Predsednik društva MIDEM
Prof. Dr. Barbara Malič, Jožef Stefan Institute, Ljubljana, Slovenia

Vice-presidents | Podpredsednika
Prof. Dr. Janez Krč, UL, Faculty of Electrical Engineering, Ljubljana, Slovenia
Dr. Iztok Šorli, Mikroiks d.o.o., Ljubljana, Slovenia

Secretary | Tajnik
Olga Zakrajšek, UL, Faculty of Electrical Engineering, Ljubljana, Slovenia

MIDEM Executive Board Members | Člani izvršilnega odbora MIDEM
Prof. Dr. Slavko Bernik, Jožef Stefan Institute, Slovenia
Assoc. Prof. Dr. Miha Čekada, Jožef Stefan Institute, Ljubljana, Slovenia
Prof. DDr. Denis Đonlagić, UM, Faculty of Electrical Engineering and Computer Science, Maribor, Slovenia
Prof. Dr. Leszek J. Golonka, Technical University, Wroclaw, Poljska
Prof. Dr. Vera Gradišnik, Tehnički fakultet Sveučilišta u Rijeci, Rijeka, Croatia
Mag. Leopold Knez, Iskra TELA, d.d., Ljubljana, Slovenia
Mag. Mitja Koprivšek, ETI Elektroelementi, Izlake, Slovenia
Asst. Prof. Dr. Gregor Primc, Jožef Stefan Institute, Ljubljana, Slovenia
Prof. Dr. Janez Trontelj, UL, Faculty of Electrical Engineering, Ljubljana, Slovenia
Asst. Prof. Dr. Hana Uršič Nemevšek, Jožef Stefan Institute, Ljubljana, Slovenia
Dr. Danilo Vrtačnik, UL, Faculty of Electrical Engineering, Ljubljana, Slovenia

Supervisory Board | *Nadzorni odbor*

Prof. Dr. Franc Smole, UL, Faculty of Electrical Engineering, Ljubljana, Slovenia
Prof. Dr. Drago Strle, UL, Faculty of Electrical Engineering, Ljubljana, Slovenia
Igor Pompe, retired

Court of honour | *Častno razsodišče*

Darko Belavič, Jožef Stefan Institute, Ljubljana, Slovenia
Dr. Miloš Komac, retired
Dr. Hana Uršič Nemevšek, Jožef Stefan Institute, Ljubljana, Slovenia

Informacije MIDEM
Journal of Microelectronics, Electronic Components and Materials
ISSN 0352-9045

Publisher / Založnik:
MIDEM Society / Društvo MIDEM
Society for Microelectronics, Electronic Components and Materials, Ljubljana, Slovenia
Strokovno društvo za mikroelektroniko, elektronske sestavne dele in materiale, Ljubljana, Slovenija

www.midem-drustvo.si